Chem Soc Rev

This article was published as part of the

2008 Chemistry at Surfaces issue

Reviewing the latest developments in surface science

All authors contributed to this issue in honour of the 2007 Nobel Prize winner Professor Gerhard Ertl

Please take a look at the issue 10 table of contents to access the other reviews

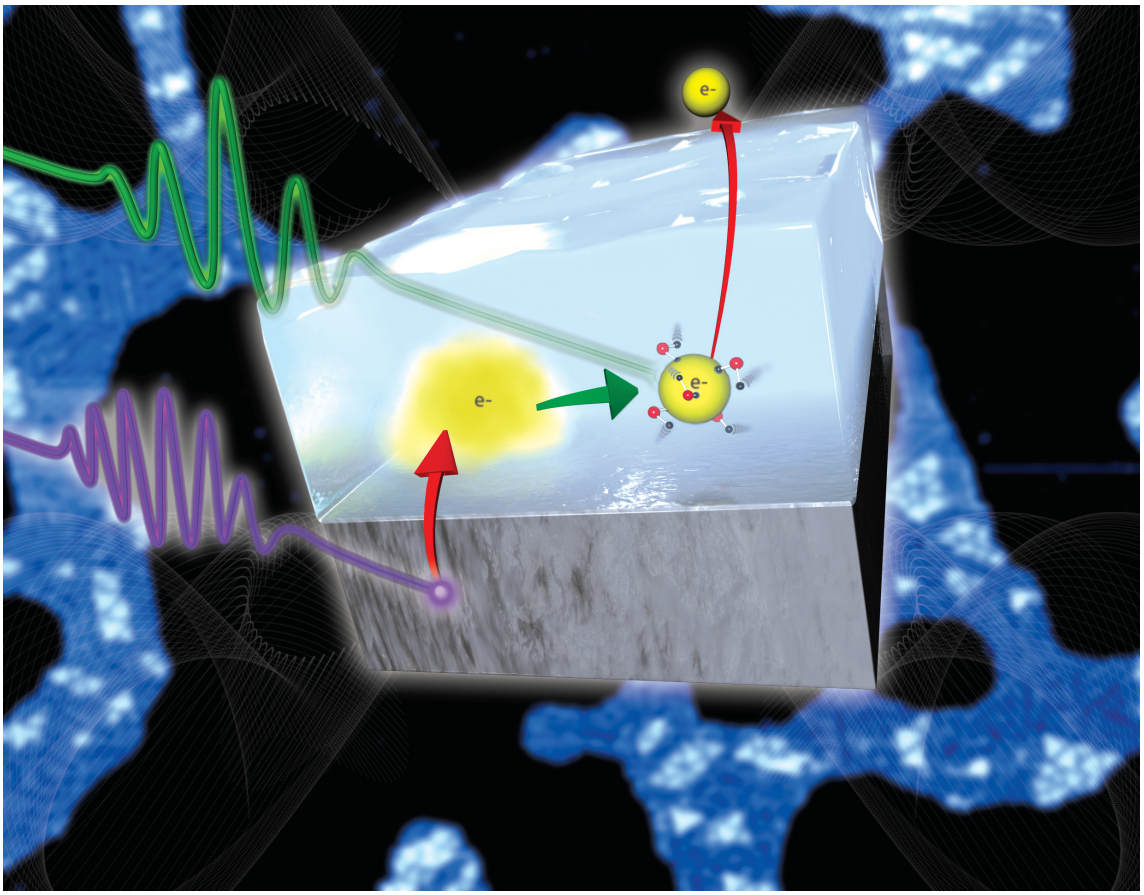

Nanoscale surface chemistry over faceted substrates: structure, reactivity and nanotemplates†‡

Theodore E. Madey,*[a] Wenhua Chen,[a] Hao Wang,[a] Payam Kaghazchi[b] and Timo Jacob*[bc]

Received 7th August 2008
First published as an Advance Article on the web 2nd September 2008
DOI: 10.1039/b719551f

Faceting is a form of self-assembly at the nanometre-scale on adsorbate-covered single-crystal surfaces, occurring when an initially planar surface converts to a "hill and valley" structure, exposing new crystal faces of nanometre-scale dimensions. Planar metal surfaces that are rough on the atomic scale, such as bcc W(111), fcc Ir(210) and hcp Re(12$\bar{3}$1), are morphologically unstable when covered by monolayer films of oxygen, or by certain other gases or metals, becoming "nanotextured" when heated to temperatures above ~700 K. Faceting is driven by surface thermodynamics (anisotropy of surface free energy) but controlled by kinetics (diffusion, nucleation). Surfaces can spontaneously rearrange to minimize their total surface energy (by developing facets), even if this involves an increase in surface area. In this *critical review*, we discuss the structural and electronic properties of such surfaces, and first principles calculations are compared with experimental observations. The utility of faceted surfaces in studies of structure sensitive reactions (*e.g.*, CO oxidation, ammonia decomposition) and as templates for growth of metallic nanostructures is explored (122 references).

1. Introduction

The emphasis of this review is on the new exploration of nanometre-scale phenomena and their influence on surface chemistry. We focus on faceted substrates that have well-characterized nanometre-scale surface features, and strive to understand how surface reactivity is affected by varying the morphology and size of surface features. Faceting, a form of self-assembly of nanometre-scale structures on adsorbate-z covered single-crystal surfaces, occurs when an initially planar surface converts to a "hill and valley" structure, exposing new crystal faces of nanometre-scale dimensions. Recent experiments, first principles calculations and applications of faceted surfaces are presented.

The formation of facets on solid surfaces is often discussed in terms of the equilibrium crystal shape (ECS) of small crystalline particles.[1–3] Examples of facet formation on

[a] *Rutgers, The State University of New Jersey, Department of Physics and Astronomy, and Laboratory for Surface Modification, 136 Frelinghuysen Road, Piscataway, NJ 08854-8019, USA*
[b] *Fritz-Haber-Institut der Max-Planck-Gesellschaft, Faradayweg 4-6, D-14195 Berlin, Germany*
[c] *Theoretische Elektrochemie, Universität Ulm, Albert-Einstein-Allee 47, D-89069 Ulm, Germany. E-mail: timo.jacob@uni-ulm.de*

† Part of a thematic issue covering reactions at surfaces in honour of the 2007 Nobel Prize winner Professor Gerhard Ertl.

‡ In memory of Professor Theodore E. Madey, who passed away on July 27, 2008 at the age of 70.

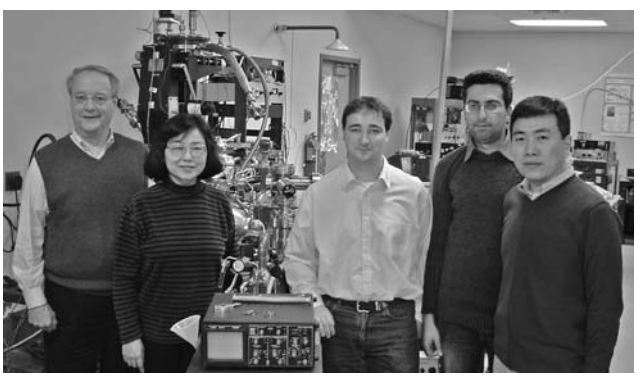

(From left to right) Theodore E. Madey, Wenhua Chen, Timo Jacob, Payam Kaghazchi and Hao Wang

Professor Theodore E. Madey is a pioneer in the field of the physics and chemistry of solid surfaces. He gained his PhD from the University of Notre Dame in 1963, after which he spent 25 years at NIST. In 1988, he became the state of New Jersey Professor of Surface Science and the Director of the Laboratory for Surface Modification at Rutgers University. Besides several prestigious awards and honours, he has received an honorary doctorate from the University of Wrocław in Poland.

Wenhua Chen is a research associate in Professor Madey's group. She received her PhD in physics from the Royal Institute of Technology, Stockholm. Her fields of research include nanoscale structure and surface chemistry.

Dr Timo Jacob is an independent research group leader at the Fritz-Haber-Institute, as well as the University of Ulm, Germany. His research interests are the theoretical modeling of interfacial systems, including the areas of electrochemistry and fuel cells.

Payam Kaghazchi is a PhD student in Dr Jacob's research group and Hao Wang in Prof. Madey's group.

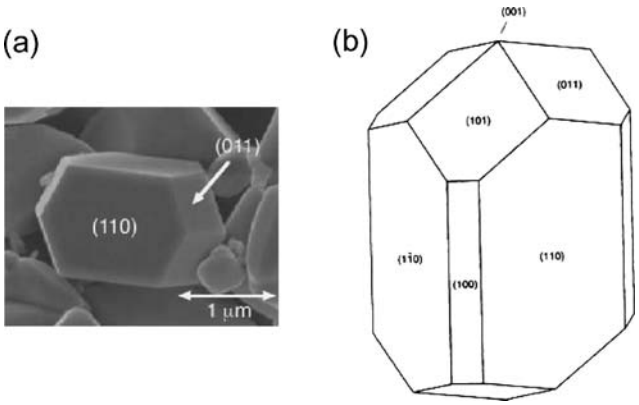

Fig. 1 (a) SEM image of rutile TiO_2 particles. Reproduced from ref. 6 by permission of The Royal Society of Chemistry on behalf of the Centre National de la Recherche Scientifique. (b) Theoretical equilibrium crystal shape (ECS) for rutile TiO_2. Reprinted with permission from ref. 7. Copyright (1994) by the American Physical Society (URL: http://link.aps.org/abstract/PRB/v49/e16721).

small crystalline particles are well documented for supported metal catalysts[4,5] and oxide nanocrystals (see Fig. 1).[6,7] Prolonged heating at elevated temperatures can cause a small particle to achieve the equilibrium shape that is dictated by the minimization of the total surface free energy, $\int \gamma dA$, where A is the surface area. Note that the specific surface free energy, γ (in J m^{-2} or eV $Å^{-2}$), is the reversible work per unit area needed to create a new surface and depends on the crystallographic orientation of the surface. The ECS is related to a polar plot of γ (the γ-plot) by the Wulff construction.[1,2] Whereas facet planes (extended flat regions of surface) are present on the equilibrium shape of small particles, the spontaneous faceting of *clean planar* metal surfaces is not commonly observed, because the anisotropy in surface free energy is generally too small for an atomically-rough surface to form facets. However, when the surface is covered by gaseous or metallic impurities, the anisotropy in surface free energy can be enhanced considerably.

A schematic of the faceting process is shown in Fig. 2. Faceting of an initially planar surface with a relatively high specific surface free energy (*i.e.*, a surface that is rough on the atomic scale, such as bcc W(111), fcc Ir(210) or hcp Re(12$\bar{3}$1)) is facilitated by the adsorption of gases and metallic monolayers (MLs). Upon heating, nanoscale features terminated by facets nucleate, grow and cover the surface. Usually, the resulting facets are more close-packed than the original planar substrate, and invariably the overall surface energy is reduced by facet formation, even though the surface area increases.[8,9]

Why is faceting of interest in surface chemistry? Somorjai and Borodko[10,11] have made persuasive arguments that a

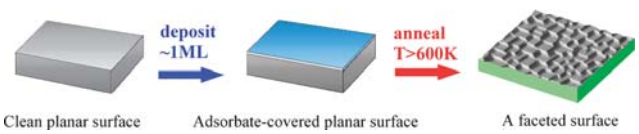

Fig. 2 A schematic of the faceting process on a planar surface. Facets form when the adsorbate-covered surface is heated and kinetic barriers are overcome.

major scientific challenge for the 21st century is to achieve a high degree of selectivity in catalysis; there is strong evidence that the geometrical and electronic structure of nanometre-scale catalyst particles play a major role in selectivity. Studies of structure sensitivity and selectivity in catalytic reactions have attracted attention for many years, and the relative roles of particle size effects, the crystallographic structure of surfaces, ensemble effects, *etc.*, have been discussed extensively. To address such issues, innovative new nanofabrication methods for assembling model catalysts at the nanometre-scale have been developed.[12] However, there are relatively few studies on the surface chemistry of nanoscale particles or surface features with specific, well-defined crystal facets and a narrow size distribution.[12–15] This is addressed in the work described here in the context of the nanoscale faceting of surfaces.

In this review, our emphasis will be on the atomically-rough surfaces of transition metals (*e.g.*, W, Mo, Ir, Rh, Re) and alloys (NiAl) that become morphologically unstable, and can undergo nanoscale faceting when covered by adsorbed gases or metallic MLs and annealed at elevated temperatures. Our focus is (a) to discuss the causes of faceting and other nanometre-scale growth phenomena on adsorbate-covered metallic (and bimetallic) surfaces, with both experimental and theoretical results being presented; (b) to correlate surface structure, surface reactivity and surface electronic properties with nanometre-scale features by model reaction studies showing structure sensitivity (*e.g.*, CO oxidation, ammonia decomposition, NO decomposition over planar and faceted Ir); (c) present evidence for the use of faceted surfaces as nanotemplates for the selective nucleation and growth of nanoscale metallic clusters. We also build on the work described in previous reviews.[2,3,8,9,16–20]

The main factor that distinguishes this work from other studies of model metallic and oxide catalysts is our emphasis on atomically-rough, high surface energy surfaces that may become morphologically unstable during typical reaction conditions. We believe that these results may be important for catalytic applications, in understanding dynamic structural rearrangements at the surfaces of high surface area catalysts and in clarifying the role of nanometre-scale size effects in surface reactions.

2. Theoretical, experimental procedures

2.A Theoretical and conceptual background

There have been important advances in the theory of faceting, ranging from atomistic studies on the process itself up to first principles and thermodynamic calculations on surface stability. Oleksy has recently applied a simple solid-on-solid model[21–24] to study the adsorbate-induced faceting of different bcc (111) surfaces.[25] Using Monte Carlo simulations and assuming a constant coverage of one physical ML, his calculations showed that the facet size increased with annealing temperature and that disordered phases became relevant at higher temperatures. Furthermore, his simulations on the faceting–defaceting transition indicated a reversible process

involving a hysteresis effect in the surface formation energy with respect to an alternating heat treatment.

Besides mesoscopic approaches, first principles electronic structure calculations have also been used to provide information on the overlayer-induced faceting of surfaces.[26–31] These studies in general showed that strongly interacting adsorbates enhanced the anisotropy in the surface free energy of both planar and faceted surfaces. Che *et al*.[26] have studied different metal overlayers on Mo(111) and found that, besides the adsorbates known experimentally to induce faceting (Pt, Pd, Au),[9,32] even Ag should lead to surface faceting. Since experimentally there is no evidence for the Ag-induced faceting of Mo(111),[33,34] they proposed that, although thermodynamically preferred, a formation barrier to nucleation prevents the surface from faceting.

Furthermore, facet formation on Ir and Re surfaces induced by oxygen and nitrogen adsorption has been studied on the basis of density functional theory calculations and thermodynamic considerations. While on Ir(210) the presence of oxygen led to the stabilization of three-sided nano-pyramids,[30,31,35] on Re(11$\bar{2}$1) and Re(12$\bar{3}$1), a variety of additional structures appeared in the corresponding phase diagrams.[36,37] These ranged from two sided-ridges to four-sided pyramids.

Although, for certain systems, contributions from edges, kinks and/or strain have been found to play a substantial role in the growth and stabilization of facets over planar surfaces,[20] the evaluation of these contributions is rather demanding for atomistic calculations, and therefore usually omitted. Consequently, so far, theoretical studies have been limited to systems that show a high enough anisotropy in surface free energy but additionally small edge and kink energies.

Besides faceting under UHV conditions, quite recently, theoretical studies were extended to electrochemical systems, where it was shown that one should also be able to realize surface faceting electrochemically by applying a proper electrode potential.[38]

2.B The thermodynamics of faceting

Since facet formation is thermodynamically driven, the important quantity is the formation energy, which can be expressed as a sum of changes in the Gibbs free energies, mainly related to surface, edge, kink and strain contributions:

$$\Delta G_{\mathrm{form}} = \Delta G_{\mathrm{surface}} + \Delta G_{\mathrm{edge}} + \Delta G_{\mathrm{kink}} + \Delta G_{\mathrm{strain}} + \ldots \quad (1)$$

Assuming the facets to be large, the overall formation energy can be approximated by the surface contribution only. This condition, usually referred as the Herring condition, is comparable to the so-called Wulff construction. On the basis of this assumption, facet formation should occur when

$$\Delta G^{\mathrm{form}} \approx \Delta G^{\mathrm{surface}} = \sum_f A_f^{\mathrm{final}} \gamma_f^{\mathrm{final}} - A^{\mathrm{initial}} \gamma^{\mathrm{initial}} < 0, \quad (2)$$

where the initial surface is characterized by the surface free energy $\gamma^{\mathrm{initial}}$ and an overall surface area A^{initial}, and the fth face of the facets accordingly by $\gamma_f^{\mathrm{final}}$ and A_f^{final}. Since, in the present case, facets showing different faces are formed on the initially planar surface after adsorption of an adsorbate (*e.g.* gaseous), eqn (2) converts into the following condition, which has to be fulfilled in order to show facet formation:

$$\frac{S_1}{\cos \vartheta_1} \cdot \gamma_1(T, p_{\mathrm{gas}}) + \frac{S_2}{\cos \vartheta_2} \cdot \gamma_2(T, p_{\mathrm{gas}}) + \cdots < \gamma^{\mathrm{initial}}(T, p_{\mathrm{gas}}). \quad (3)$$

Here, the parameters S specify the partial contributions of the different faces to each nano-shaped facet, while ϑ are the tilt angles of the faces with respect to the initial substrate, T is the temperature and p_{gas} is the partial pressure of the surrounding gas, whose adsorption induces the faceting. While all previously mentioned parameters are either given by the experimental conditions (*i.e.*, T and p_{gas}) or can be obtained by geometrical considerations (*i.e.*, S and ϑ), the remaining information required for eqn (3) are the surface free energies of the initial substrate, as well as the faces of the final facets.

To evaluate the different surface free energies relevant to eqn (3), the *ab initio* atomistic thermodynamics approach can be used, which allows one to evaluate the stability of surfaces/interfaces that are in contact and in thermodynamic equilibrium with a surrounding atmosphere.[31,39–41] The most relevant surface structures are then characterized by a low surface free energy; as an example, for an interface between an Ir surface and gaseous oxygen, this can be written as

$$\gamma(T, p_{\mathrm{O_2}}) = \frac{1}{A}[G(T, p_{\mathrm{O_2}}) - N_{\mathrm{Ir}} \mu_{\mathrm{Ir}}^{\mathrm{bulk}} - N_{\mathrm{O}} \mu_{\mathrm{O}}^{\mathrm{gas}}(T, p_{\mathrm{O_2}})]. \quad (4)$$

Here, G is the Gibbs free energy of the particular slab, A is the corresponding surface area, and $\mu_{\mathrm{Ir}}^{\mathrm{bulk}}$ and $\mu_{\mathrm{O}}^{\mathrm{gas}}$ are the chemical potentials of both reservoirs the system is assumed to be in contact with, *i.e.* the Ir bulk and gaseous oxygen. Since the temperature and pressure dependence of all solid phases (surfaces and bulk) is small compared to those of gaseous phases, the oxygen chemical potential, which is given by

$$\mu_{\mathrm{O}}^{\mathrm{gas}}(T, p_{\mathrm{O_2}}) = \frac{1}{2}\left[E_{\mathrm{O_2}}^{\mathrm{tot}} + \bar{\mu}_{\mathrm{O_2}}(T, p^0) + k_{\mathrm{B}} T \ln\left(\frac{p_{\mathrm{O_2}}}{p^0}\right)\right], \quad (5)$$

dominates the T and p dependence of the surface free energies. Here $E_{\mathrm{O_2}}^{\mathrm{tot}}$ is the calculated total energy of an isolated O_2 molecule and $\bar{\mu}_{\mathrm{O_2}}(T, p^0)$ is the standard chemical potential at temperature T, which includes all the contributions from vibrations and rotations of the molecule, and the ideal gas entropy at 1 atm.

With eqn (4), it is possible to evaluate the interfacial free energies of the different surface faces of the facets, since all relevant quantities can be deduced from first principles. For the faceting of Ir and Re surfaces that are discussed later, density functional theory calculations were used, together with eqn (3), to finally obtain a surface phase diagram for surface faceting (*e.g.* see section 3.B.a).

2.C Experimental methods

An array of ultrahigh vacuum (UHV) surface science methods have been used for most of the faceting studies described here. In such cases, the surfaces are cleaned in a UHV, gases and other adsorbates are deposited, and the surface is heated to

induce the formation of facets. In some cases, faceting is studied in real time at an elevated temperature, but for most systems, facets are identified after the heated sample is cooled and the facets have been "frozen in". Exact details are given in the respective papers. Methods for characterizing structure and morphology include high resolution scanning tunneling microscopy (STM), atomic force microscopy (AFM), low energy electron diffraction (LEED) and scanning electron microscopy (SEM). LEED is especially useful for screening candidate surfaces to determine whether or not facets form.[42,43] In a typical LEED experiment, the sample is mounted with its average surface (approximately) normal to the incident electron beam. As the incident electron energy increases, LEED beams from a planar substrate converge on the specular (0,0) beam, which is usually in the center of the pattern; in contrast, LEED beams from a faceted surface converge on specular beams (0,0)-scattered from the facets in directions away from the pattern center.

Nucleation, growth and relaxation kinetics are studied using variable temperature STM (VT-STM) and low energy electron microscopy (LEEM).[44,45] Surface chemistry measurements are based on temperature-programmed desorption (TPD) spectroscopy,[35,46] high resolution electron energy loss spectroscopy (HREELS),[47] catalysis in a UHV-compatible reactor for surface chemistry and Auger electron spectroscopy (AES). Field electron emission microscopy (FEM) and field ion microscopy (FIM) have been used to study the faceting of curved surfaces with nanometre-scale dimensions.[48,49] Synchrotron radiation methods have been invaluable for determining the electronic properties and growth structure/statistics *via* soft X-ray photoemission spectroscopy (SXPS),[50–52] scanning photoelectron microscopy (SPEM),[53] grazing incidence X-ray diffraction (GIXD) and grazing incidence small angle X-ray scattering (GISAXS).[54]

In addition to UHV studies, there has been recent work on oxide and other surfaces, in which facets are formed by heating the samples in a high temperature oven ($\sim$1000 °C), in air, at 1 atm.[55] Such surfaces offer potential as nanotemplates for the assembly of nanoparticles, nanowires or biomolecules on surfaces from solution. Another interesting procedure for generating faceted surfaces has been reported recently: the faceting of an initially planar Ir(210) surface was found to occur in an electrochemical cell using a Cl-containing electrolyte.[56]

3. Faceting phenomena

3.A The general characteristics of faceting

Before discussing specific faceted surfaces, we begin by summarizing several general characteristics of faceting.

(1) As indicated in the Introduction, the faceting of initially planar surfaces is facilitated by the adsorption of gases or metallic MLs that enhance the anisotropy of the surface free energy. The adsorbed layers act as surfactants coating the surface, and the substrate reconstructs to form faceted structures that are themselves coated by the adsorbed layer. The development of faceted structures on surfaces demonstrates that the minimum in surface free energy does not imply a minimum in surface area; the surface area of faceted substrates is often a few percent higher than that of the original planar substrate. When 3-D faceted features appear, the surfaces of the facets are generally more close-packed and invariably have a lower overall surface free energy than the initial atomically-rough planar surface.

(2) A fundamental constraint on faceting is the conservation of total surface (substrate) symmetry.[18] Surfaces with low Miller indices often have a high symmetry that is reflected in the symmetry of the faceted surfaces (*e.g.*, the C_{3v} W(111) substrate develops three-sided pyramids with {211} facets and the C_{1h} Ir(210) substrate, with its single reflection plane, develops elongated three-sided pyramids with one (110) and two {311} facets, *etc.*). To maintain the overall symmetry of the original surface, whether it has high symmetry or simply C_1 symmetry, symmetry-equivalent facets must form.[18]

(3) Although faceting is driven by thermodynamics, *i.e.*, the minimization of surface free energy, it is controlled by kinetic barriers (*i.e.*, the kinetics of diffusion and nucleation), meaning that mass transport generally limits facet growth. In general, there is a material-dependent "temperature window" within which facets are observed. At low temperatures, an adsorbate-covered surface can be metastable; as the temperature increases, kinetic barriers to diffusion and nucleation are overcome and facets form. Facet sizes increase over a limited range of temperatures as the edge energy is minimized. At high temperatures, the desorption of adsorbates and/or temperature-dependent surface free energies reduce the anisotropy of γ, and the surface relaxes back to planar.

(4) Both homogeneous and heterogeneous nucleation and growth of facets are observed. Homogeneous nucleation means that when a critical surface coverage is attained and the temperature is sufficient, the surface spontaneously develops nanometre-scale faceted features over its entire area. Nucleation may be accompanied by a pre-roughening, but the entire surface ultimately develops facets. Such behavior is widely observed for surfaces of W, Mo, Re, Ir, Pt, Cu, *etc.*[8,9,18,42,43,46,57,58] In contrast, heterogeneous nucleation means that facets form in coexistence with large planar regions, and there appear to be specific sites where facet nucleation occurs. For instance, in the case of the oxygen-induced faceting of NiAl, relatively large pyramids (>100 nm) are separated by hundreds of nm, and may be associated with the nucleation of oxide structures at specific sites. Faceting on α-$Al_2O_3(10\bar{1}0)$ also starts with the nucleation and growth of individual isolated facets.[59]

3.B Adsorbate-induced faceting: structural aspects

There is extensive literature that describes how the faceting of initially planar surfaces is facilitated by the adsorption of gases and metallic MLs that enhance the anisotropy of the surface free energy.[18] Except for our recent studies of faceting in bimetallic systems,[8,9,16,60–63] there have been relatively few other reports of faceting induced by metals-on-metals.[19,48,64–66] However, there are many papers on the faceting of metals induced by gaseous impurities or other non-metallic impurities, as well as on the faceting of semiconductors under a variety of conditions. Surfaces for which

adsorbate-induced faceting has been observed include nanoscale supported catalysts,[5,65,67] vicinal Cu surfaces,[68–70] O/Ir(210),[42] O and Cl/W(111) and O/Mo(111),[19,49,71–75] O/Re(12$\bar{3}$1),[43] O/Re(11$\bar{2}$1),[36] N/Re(11$\bar{2}$1),[36] N/Fe(111),[76] Au-covered vicinal Si,[77] Cl/Ag(111),[78] O/Pt(210),[57,79] O/Rh(210),[80,81] O/NiAl(111)[82] and CO and O/Pt(110)[83] at high pressure, activated nitrogen on Cu(210) and Ni(210),[84,85] and even CO/Ni(110) at high pressure and temperature.[86] Fluctuations and bistabilities reported for the various catalyst nanoparticles[87] may also be associated with dynamic surface restructuring in the presence of reactant gases. In the present review, we will focus on a few illustrative examples from our own work to illustrate the range of faceting phenomena.

3.B.a The oxygen-induced faceting of metals. While many specific adsorbate/substrate combinations may lead to substrate faceting, oxygen is the adsorbate most likely to cause the faceting of metals and semiconductors; moreover, the surfaces of bulk oxides often develop facets upon annealing. An increasing complexity is observed in the morphology of faceted surfaces in going from Ir and Rh, through W and Re, to a NiAl alloy surface: a complexity that apparently scales with the heat of oxide formation. In the following paragraphs, we will discuss examples of oxygen-induced faceting and show how theory can contribute to the understanding of the observations.

The oxygen-induced faceting of Ir, Rh and Pt. The three metals Ir, Pt and Rh all form reducible oxides with relatively low heats of formation. Their O-covered surfaces can be reduced by H_2 or CO, and all have surfaces that have been found to facet. For example, oxygen is found to chemisorb dissociatively onto Ir(210) at room temperature. When atomically-rough Ir(210) is covered with more than a 0.5 ML of oxygen and annealed, pyramidal facets develop on the initially planar surface.[42,88] When annealed to 600 K, the O-covered Ir(210) surface forms faceted (triangular pyramidal) structures with {311} and (110) faces; the surface remains faceted for substrate temperatures, T, below 850 K (see Fig. 3). If T reaches approximately 850 K, the substrate structure reverts to the O-covered (210) planar state and does so reversibly, provided that oxygen is not lost due to desorption or *via* chemical reactions, upon which the planar (210) structure remains.

The facet size increases with annealing temperature and upon varying the annealing conditions. STM data show that facets having mean sizes ranging from 5 to 14 nm can be generated. In separate LEEM studies, facet sizes to a maximum of $\sim$25 nm are observed.[45] The LEEM data also demonstrate that facets nucleate and grow uniformly over the entire surface, without evidence for ''patches'' of facets coexisting with planar regions, as seen for the Pt/W(111) system.[44] LEEM offers a unique microscopic view of the faceted surface, with a lateral resolution ($\sim$7 nm) that permits the observation of growth dynamics.

The O-covered {311} facets are smooth and unreconstructed, while the larger (110) facets consist of unreconstructed terraces and restructured areas that exhibit a complex superstructure on an atomic scale (Fig. 3). The

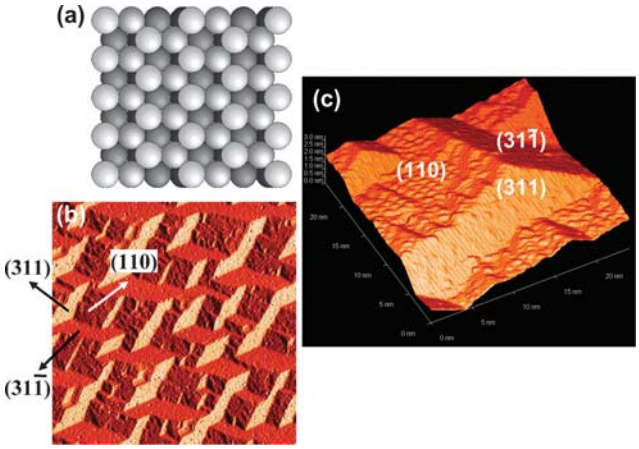

Fig. 3 (a) The surface structure of Ir(210). (b) STM derivative image (100 nm $\times$ 100 nm) of O-covered faceted Ir(210) prepared by flashing Ir(210) in O_2 (5×10^{-8} Torr) to $T > 1700$ K and subsequent cooling it in O_2 to 300 K. Following a flash annealing in O_2, facets form as the crystal cools below $\sim$1150 K. Reprinted with permission from ref. 46. Copyright (2005) American Chemical Society. (c) STM scan (24 $\times$ 24 nm) of one pyramid of O-covered faceted Ir(210), showing the superstructure on the (110) facet. Reprinted from ref. 122 with permission from the author and ProQuest LLC.

superstructure is proposed to be a ''stepped double missing row'' (110) surface or a reconstructed (320) surface.

In recent experiments, the oxygen-induced faceting of Rh(210) has also been observed.[81] O-covered Rh(210) undergoes a massive reconstruction to form three-sided nanoscale pyramids characterized by two {731} facets and a ($n \times 1$) reconstructed (110) facet. The results agree with LEED studies by Tucker,[80] which were among the first reports of faceting ever published. Voss and Kruse[89] have reported the O-induced faceting of Rh field emission tips. It is interesting to note the contrast between the faceting of Ir(210) and Rh(210) with Pt(210). For both Ir(210) and Rh(210), the faceted structures are three-sided pyramids, while on Pt(210), long ridges, consisting of sides with (110) and (310) facets, are reported by Ertl and colleagues;[57] subtle differences between the free energies of the O-covered surfaces must be at play.

In addition, as indicated schematically in Fig. 4, oxygen can be removed from the faceted Ir(210) and Rh(210) surfaces while preserving (''freezing'') the faceted structure through the use of low temperature chemical cleaning methods (CO

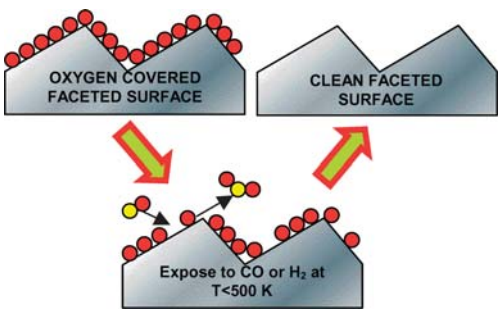

Fig. 4 Schematic of the process used to prepare a clean faceted surface. When adsorbed, the O_2 is removed from faceted Ir and Rh by a reaction at low T (<500 K); the clean facets remain ''frozen''.

oxidation, or reaction of H_2 to form H_2O).[42,47] The resulting clean faceted surfaces remain stable while $T < 600$ K. For temperatures above this value, the clean surface irreversibly relaxes to the planar state. Below, in section 3.C, the use of clean faceted Ir in studies of surface chemistry is presented.

Theoretical studies on the oxygen-induced faceting of Ir(210). In order to evaluate the stability of planar and faceted Ir(210), eqn (3) of section 2.B can be used, where the surface free energy of each face is given by eqn (4), assuming that the main temperature and pressure dependence is dominated by the oxygen chemical potential (eqn (5)). Since this approach is based on the Herring condition, in which contributions from step-edges, kinks and surface stress or strain are considered to be small, one can separately calculate the adsorption of oxygen on all surface orientations involved in the faceting; these being Ir(210), Ir(311) and Ir(110). Besides regular Ir(110), this also includes the "stepped double-missing-row" superstructure that had been observed on the (110) faces of the nanopyramids following annealing at higher temperatures.[88]

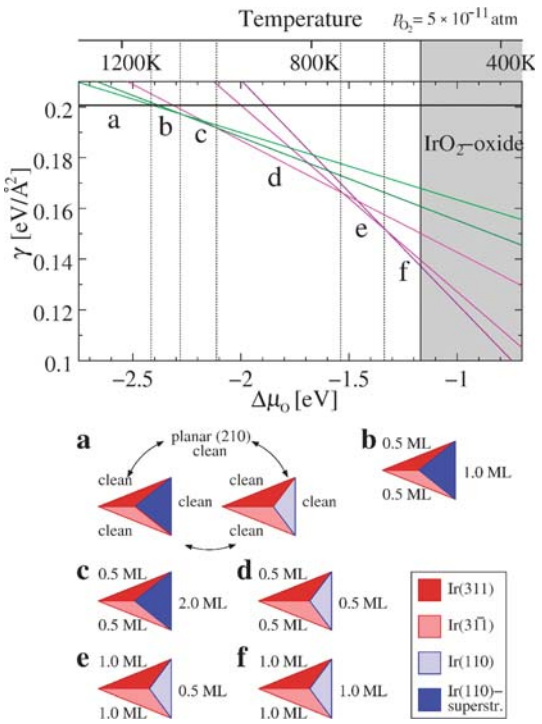

Fig. 5 Surface phase diagram for the faceting of planar Ir(210), showing the surface free energy, γ, as function of the oxygen chemical potential, referenced as $\Delta\mu_O = \mu_O^{gas} - \frac{1}{2}E_{O_2}^{tot}$. It combines clean and oxygen covered planar Ir(210), as well as two types of three-sided nanopyramids: (311)/(31$\bar{1}$)/(110)- and (311)/(31$\bar{1}$)/(110)-superstructures. The models below the phase diagram show the surface morphologies in the oxygen chemical potential ranges indicated. The oxygen coverages for the different faces of the nanopyramids given for each model are defined such that 1 ML is always one oxygen atom per (1 × 1) unit cell of the corresponding surface orientation (*i.e.*, a geometric monolayer). For comparison with experiment, the oxygen chemical potential scale has been converted to a temperature scale (given above the phase diagram) for $p_{O_2} = 5 \times 10^{-11}$ atm. Reprinted with permission from ref. 30. Copyright (2008) American Chemical Society.

On the basis of density functional theory calculations for the different clean and O-covered surfaces,[90] described in detail in ref. 30, the full phase diagram for surface faceting shown in Fig. 5 could be generated. There, we can distinguish between clean and O-covered surfaces of (i) planar Ir(210), (ii) nanopyramids with (311)-, (31$\bar{1}$)- and (110)-regular faces, and (iii) nanopyramids with (311)-, (31$\bar{1}$)- and (110)-superstructure faces. Furthermore, the chemical potential was converted to a temperature scale for $p_{O_2} = 5 \times 10^{-11}$ atm, since most facet formation experiments have been conducted under this pressure.

The surface phase diagram shows that at this pressure and for temperatures above 1130 K, no oxygen is adsorbed on the surface. Although, for the clean surfaces, the calculations reveal a slightly higher stability of the facets compared to planar Ir(210), the difference of only 3 meV Å^{-2} is within calculation error. Furthermore, contributions from step-edges and kinks, which had been omitted, destabilize the facets, finally leading to the conclusion that at higher temperatures, the surface should be clean planar Ir(210). This is also in agreement with the experimental observation of a phase transition from clean faceted Ir(210) to clean planar Ir(210) at temperatures above $\approx$600 K.[42]

Below 1130 K, the phase diagram indicates that the adsorption of oxygen takes place, causing the formation or stabilization of the nanofaceted surface. This temperature is in good agreement with the experimental value of $\sim$1150 K,[46] showing that by combining experiment and theory, a deeper insight into surface faceting can be obtained. While facets formed at higher temperatures consist of (311)-, (31$\bar{1}$)- and (110)-superstructure faces, the (110)-superstructure appears to be replaced by regular unreconstructed (110) for facets formed at lower temperatures, leading to (311)/(31$\bar{1}$)/(110)-regular facets. Reducing the temperature leads to an increased oxygen coverage on the different facet faces, but does not modify the structure any further until IrO_2 bulk oxide appears as a stable phase below $T = 575$ K. Note that in each temperature range (or chemical potential), the curve with the lowest value of γ corresponds to the predicted stable structure.

Interestingly, the presence of the (110)-superstructure face at temperatures of 1130 K $> T >$ 1000 K is rather remarkable. On a planar Ir(110) surface, this superstructure is always less favorable than regular (110),[91] but this is different for the faceted Ir(210) surface. There, the superstructure forms on the (110)-side of the nanopyramids at higher temperatures, which is a consequence of the non-linear dependency of the surface free energy on the tilt angle (see the prefactors on the left side of eqn (3)) and the fact that the (110) faces of the nanopyramids are already tilted with respect to the (210) substrate.

The oxygen-induced faceting of Re: a comparison with nitrogen-induced faceting. To complement our studies on the faceting of atomically-rough fcc surfaces, we have characterized the faceting of two atomically-rough hcp Re surfaces having (12$\bar{3}$1) and (11$\bar{2}$1) orientations (Fig. 6). For Re, a hcp metal, little is known about its faceting behavior, although it is an important component of many catalysts.[92–94] Re has a higher heat of oxide formation than Ir, Rh or Pt, and the faceting is considerably more complicated. We observed a complex

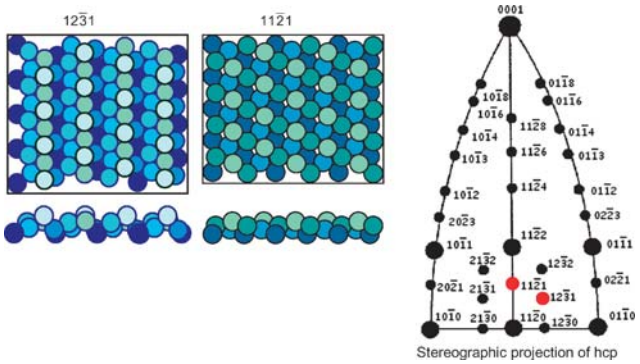

Fig. 6 The surface structures (bulk truncated) of ideal hcp Re(12$\bar{3}$1) and Re(11$\bar{2}$1), and a stereographic projection of the hcp lattice on the (11$\bar{2}$0) plane.

morphological evolution of faceting on Re(12$\bar{3}$1) when the surface was covered by oxygen at 300 K and annealed at $T > 700$ K. Depending on the oxygen coverage and annealing temperature, no fewer than five distinct facets with different orientations appeared![37,43] As shown in Fig. 6, the Re(12$\bar{3}$1) surface was atomically-rough with six layers of atoms exposed. It also has a relatively high surface free energy and a high probability of forming facets when covered by certain adsorbates and then annealed.

The morphology of the faceted surface depends on the initial oxygen coverage on Re(12$\bar{3}$1), and the evolution of facets is related to the change of surface energy anisotropy due to the adsorption of oxygen. When oxygen coverage, θ, is between 0.7 and 0.9 ML, long ridges formed by (01$\bar{1}$0) and (11$\bar{2}$1) faces emerge on Re(12$\bar{3}$1) upon annealing.[43] A LEED experiment that illustrates the ridge-like structures is shown in Fig. 7;[43] a corresponding STM image is also shown. For 0.9 ML $< \theta <$ 1 ML, the ridges become truncated by a third face, (10$\bar{1}$0), which has the same surface structure as (01$\bar{1}$0) but a higher tilt angle with respect to (12$\bar{3}$1).[43] When Re(12$\bar{3}$1) is fully covered by oxygen (θ = 1 ML), a fourth face (01$\bar{1}$1) also emerges upon annealing (Fig. 8).[43] The spatial relationship between Re(12$\bar{3}$1) and all the observed facets is shown in the stereographic projection plot of the hcp lattice in Fig. 6 (above). It is not surprising that (01$\bar{1}$0), (10$\bar{1}$0) and (01$\bar{1}$1) appear as faces because they all have rather smooth surfaces and thus low surface free energies. No further changes in morphology are observed after larger doses of oxygen at 300 K, followed by annealing.

In contrast to the behavior observed at room temperature,[43] the (11$\bar{2}$1) face completely disappeared and the new (10$\bar{1}$1) face emerged, together with the other three faces, when Re(12$\bar{3}$1) was exposed to >120 Langmuir (L, 1 L = 10^{-6} Torr s = 1.33 $\times$ 10^{-4} Pa s) of oxygen between 800 and 1000 K.[37] The disappearance of the metastable (11$\bar{2}$1) face and the appearance of this (10$\bar{1}$1) face is correlated with the formation of oxidized Re, Re_2O_3, as revealed by HRSXPS studies.

We also chose to study the metastable Re(11$\bar{2}$1) crystal surface. As described above, Re(11$\bar{2}$1) is morphologically unstable after annealing high coverages of O onto faceted Re(12$\bar{3}$1). For initially planar Re(11$\bar{2}$1), the adsorption of oxygen at room temperature, followed by annealing at

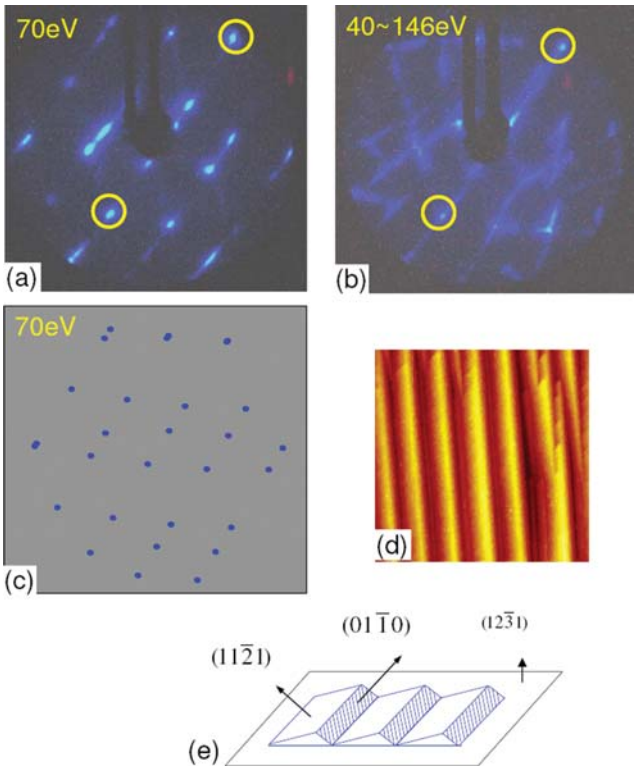

Fig. 7 An example of the use of LEED for facet identification. LEED patterns of a faceted O/Re(12$\bar{3}$1) surface formed by dosing 3 Langmuir (L, 1 L = 10^{-6} Torr s = 1.33 $\times$ 10^{-4} Pa s) O_2 (0.9 ML O) at 300 K followed by annealing at 900 K. (a) E_e = 70 eV. (b) E_e varies from 40 to 146 eV. The circles in (a) and (b) indicate specular beams from the facets. (c) The kinematic simulation of (a). Reprinted with permission from ref. 43. Copyright (2006) by the American Physical Society (URL: http://link.aps.org/abstract/PRB/v74/e205426). (d) STM image (150 $\times$ 150 nm) of a faceted O/Re(12$\bar{3}$1) surface prepared by flashing in O_2 (1 $\times$ 10^{-7} Torr).[36] (e) A schematic model of the faceted surface.

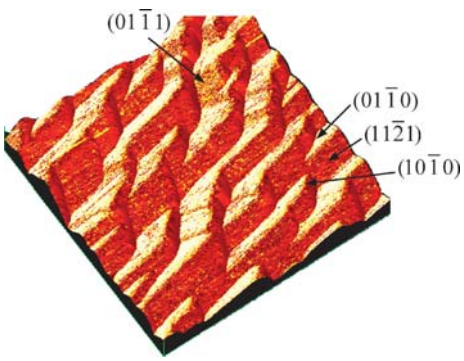

Fig. 8 STM image (50 $\times$ 50 nm) of the faceted Re(12$\bar{3}$1) surface prepared by dosing 10 L O_2 at 300 K and annealing at 900 K.[36] The facets exposed include (11$\bar{2}$1), (01$\bar{1}$0), (01$\bar{1}$1) and (10$\bar{1}$0).

elevated temperatures, caused the surface to become partially faceted with (01$\bar{1}$0) and (10$\bar{1}$0) faces, forming zigzag chains (Fig. 9).[36] Under oxidation conditions, *i.e.* dosing a large amount of oxygen at high temperatures (900–1000 K), the (11$\bar{2}$1) surface was completely covered by four-sided nanoscale pyramidal structures, whose facets were identified as (01$\bar{1}$0),

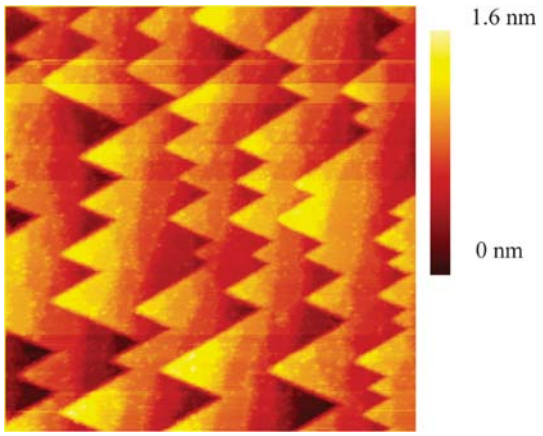

Fig. 9 STM image (100 × 100 nm) of the partially faceted Re(11$\bar{2}$1) surface, prepared by dosing 10 L O_2 at 300 K and annealing at 1000 K.[36]

(10$\bar{1}$0), (01$\bar{1}$1) and (10$\bar{1}$1).[36] In contrast, after exposure to ammonia at 700 K, the Re(11$\bar{2}$1) surface exhibited a (1×2) reconstruction and remained planar (ammonia dissociates on Re, and only N remains on the surface at $T > 600$ K).[36] Upon exposure to ammonia at 900 K, the Re(11$\bar{2}$1) surface became completely faceted, forming two-sided ridge-like structures (Fig. 10);[36] the orientations of the ridge sides were (13$\bar{4}$2) and (31$\bar{4}$2), which were different from *any* of the facets found in the oxygen-induced faceting of Re(12$\bar{3}$1) and Re(11$\bar{2}$1).

Our work with Re demonstrates the complexity of surface morphology in the adsorbate-induced faceting of hcp metal surfaces and has important implications for Re-based catalysts that operate under oxygen-rich or nitrogen-rich conditions, the structure of the catalysts often affecting their performance. Moreover, it is possible to tailor the surface morphology by choosing the appropriate adsorbate, adsorbate coverage and annealing conditions, which in turn provides different but related model systems to study structural sensitivity in catalytic reactions as well as potential templates to grow nanostructures.

Theoretical studies on the N-induced faceting of Re(11$\bar{2}$1). Similar to the oxygen-induced faceting of Ir(210), where the theoretically obtained phase diagram showed that, under certain coverage and environmental conditions, nanofacets become thermodynamically stable (see section 3.B.a and Fig. 5), in the case of Re(11$\bar{2}$1), equivalent studies confirmed the experimental observation that by properly choosing the adsorbate and heat treatment, different nanofacets could be generated.[95] Fig. 11 shows the corresponding phase diagram for Re(11$\bar{2}$1) in contact with a nitrogen atmosphere. This phase diagram was generated on the basis of density functional theory calculations for different clean and adsorbate-covered surfaces involved in faceting and observed experimentally.[96] These included planar Re(11$\bar{2}$1) as the initial substrate, and Re(13$\bar{4}$2)/Re(31$\bar{4}$2) facets that were observed to form two-sided ridges after nitrogen adsorption (*cf.* STM image in Fig. 10). Note that N was deposited on Re(11$\bar{2}$1) using gaseous NH_3 in the experiments of Fig. 10,[36] whereas the phase diagram of Fig. 11 is based on the adsorption of nitrogen from N_2. However, it occurs that nitrogen atoms that are adsorbed on Re(11$\bar{2}$1) recombine to N_2 upon desorption, so we could assume that the system was in

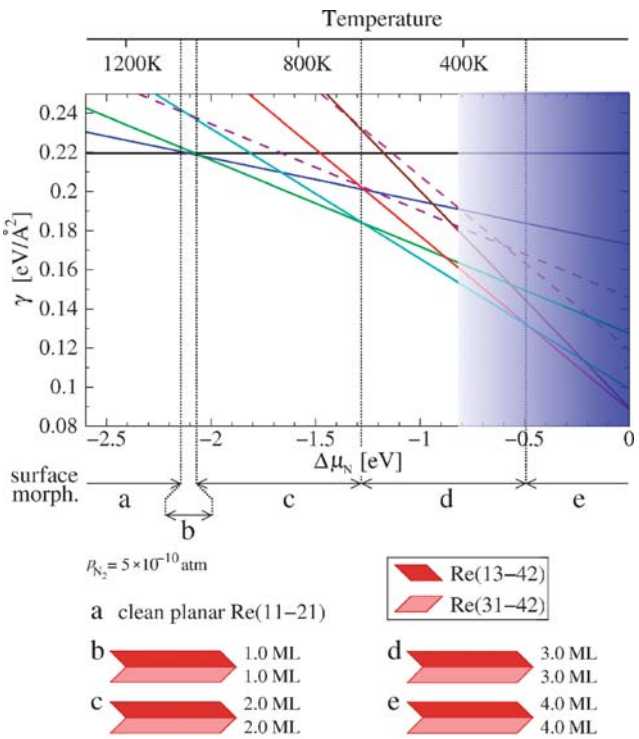

Fig. 11 Surface phase diagram for the nitrogen-induced faceting of planar Re(11$\bar{2}$1),[95] showing the surface free energy as a function of the nitrogen chemical potential, referenced as $\Delta\mu_N = \mu_N^{gas} - \frac{1}{2}E_{N_2}^{tot}$. The models below the phase diagram sketch the surface morphologies in the nitrogen chemical potential ranges indicated below the phase diagram. Nitrogen coverages given with each model (below) are again in geometrical MLs, *i.e.* 1 ML is defined as one adsorbate atom per (1 × 1) unit cell of the corresponding surface orientation. Since the phase diagram is not valid for high nitrogen chemical potentials, where formation of Re nitride is expected, this part is shaded. Dashed lines correspond to planar N/Re(11$\bar{2}$1) with different adsorbate coverages. For comparison with experiment, the $\Delta\mu_N$ scale has been converted to temperatures (given above the phase diagram) for $p_{N_2} = 5 \times 10^{-10}$ atm.

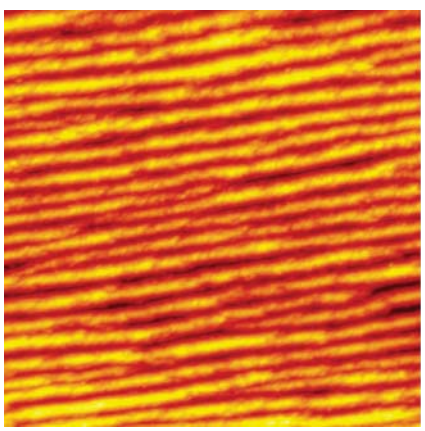

Fig. 10 STM image (100 × 100 nm) of the faceted Re(11$\bar{2}$1) surface, prepared by exposing to ammonia at 900 K.[36] The ridges have {13$\bar{4}$2} orientations.

thermodynamic equilibrium with N_2; thus the nitrogen chemical potential remains unchanged in Fig. 11.

The N/Re(11$\bar{2}$1) phase diagram (Fig. 11) shows that, at nitrogen partial pressures of $p_{N_2} = 5 \times 10^{-10}$ atm and above approximately 1080 K, no nitrogen is adsorbed onto the surface, leading to clean planar Re(11$\bar{2}$1) as the stable surface morphology. Below this temperature, nitrogen adsorption occurs, which immediately causes facet formation. The nanofacets that become stabilized are two-sided ridges combining nitrogen-covered Re(13$\bar{4}$2) and Re(31$\bar{4}$2) faces. Interestingly, even considering the uncertainties of the method and the phase diagram (see section 2.B), the nanofaceted surface thus formed is significantly more stable than the planar nitrogen-covered Re(11$\bar{2}$1) surface (see dashed lines in Fig. 11). Lowering the temperature only increases the nitrogen coverage on the ridges, but does not modify the surface morphology any further. Both conclusions are in agreement with experiment.

A phase diagram has been obtained for the oxygen-induced faceting of Re(11$\bar{2}$1) and shows considerable variety in possible surface morphologies due to energetically-close phases. The details of the O/Re(11$\bar{2}$1) phase diagram will be described in forthcoming papers.[95,97]

The oxygen-induced faceting of tungsten. Many years ago, in LEED studies by Taylor,[98] and by Tracy and Blakely,[73,74] it was recognized that oxygen induces the faceting of tungsten surfaces. In particular, the initial faceting of W(111) was characterized by the growth of {112} facets. Fig. 12(a) shows an STM image of the three-sided pyramids, with symmetric {112} facets, that formed after heating W(111) exposed to a low dose of oxygen (0.5 L O_2).[49] To illustrate the effects of the oxidation of the O/W system, the image in Fig. 12(b) corresponds to W(111) after heating in oxygen at 1200 K, followed by annealing at 1375 K.[99] It appears that annealing under conditions where tungsten oxides form leads to a greatly increased complexity on the nanofaceted surface,[99] similar to the case of Re described above.

Oxygen-induced faceting on NiAl(111). Alumina is one of the most frequently used oxide supports for transition metals in heterogeneous catalysis. Our research is focused on the O-induced faceting of NiAl(111) and is motivated by the possibility that an alumina thin film-covered faceted NiAl surface may be an interesting substrate for model studies of alumina-supported metal catalysts.

The atomically-rough NiAl(111) surface remained planar at room temperature when exposed to oxygen. However, the O-covered surface changed its morphology and became partially faceted upon annealing at $\geq$ 1100 K. Nucleation and growth of nanoscale pyramids with {110} facets were observed at spatially-separated locations. The facets coexisted with planar O-covered NiAl(111)[100] (see Fig. 13(a)). The adsorption and reaction of oxygen on NiAl(111) were characterized by the HRSXPS measurements of Al 2p and Ni 3p core levels for the faceted and planar surfaces.

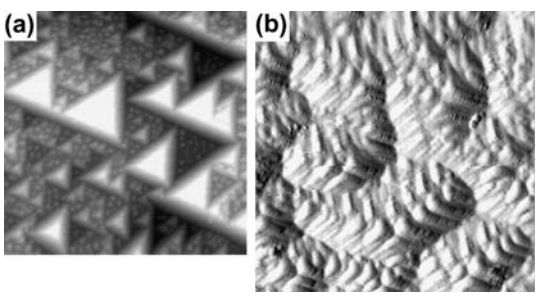

Fig. 12 (a) STM image (50 × 50 nm) of O-covered faceted W(111) prepared by exposure to 0.5 L O_2 at 300 K, followed by annealing at 1075 K for 3 min. Reprinted from ref. 49 with permission from Elsevier. (b) STM derivative image (20 × 20 nm) of O/W(111) prepared by heating with 60 L O_2 at 1200 K, followed by annealing at 1375 K. Reprinted from ref. 99 with permission from the author and ProQuest LLC.

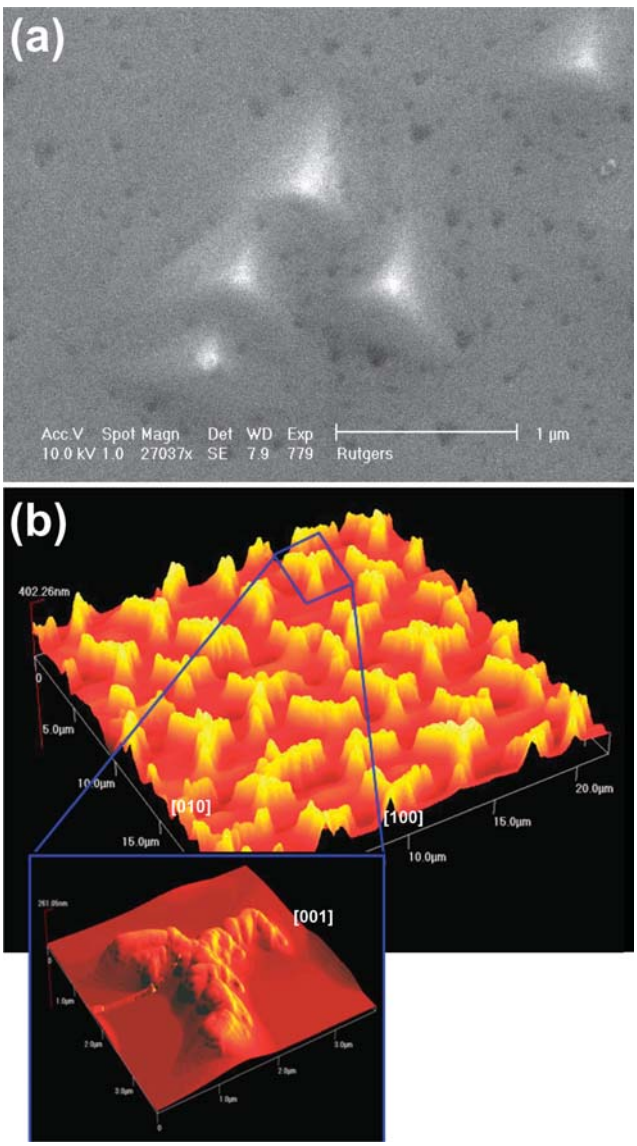

Fig. 13 (a) SEM image of O/NiAl(111) after oxidation at 300 K and further annealing at 1100 K. Reprinted from ref. 100 with permission from the author. (b) AFM image of features on NiAl(111) after repeated exposure to O_2 and annealing. In-plane, each feature extends several micrometres and is 250–400 nm high. Reprinted from ref. 82 with permission from Elsevier.

Moreover, after prolonged exposure to oxygen, followed by annealing at elevated temperatures, unusual 3-D features exhibiting three-fold symmetry erupted from the surface and were oriented along low index <010> directions (see Fig. 13(b)), their dimensions being several micrometres in length and 250 to 400 nm in height. An SEM X-ray mapping study indicated that these were spinel ($NiAl_2O_4$) structures.[82] Loginova *et al.*[53] characterized the features at the Elettra synchrotron in Italy, using their unique micro-XPS system (SPEM) to study the surface composition of the features in Fig. 13(b) with a 200 nm lateral resolution. The results were consistent, identifying the features as $NiAl_2O_4$ spinel. A proposed qualitative model of spinel formation is as follows. After oxidation of the surface, oxygen diffuses below it upon annealing. Aluminium oxide may nucleate together with Ni-rich regions in the bulk, the subsurface nucleation of $NiAl_2O_4$ spinel taking place at the Al_2O_3/Ni interface. After repeated cycles of oxidation and annealing, the spinel clusters grow and, upon reaching a critical size, their lattice strain is relieved by eruption of the spinel structures above the surface. These results may have interesting implications for another catalytic system, where aluminium oxide is combined with high area Fe in ammonia synthesis catalysts. The oxidized aluminium acts as a "structural promoter" to inhibit sintering of the Fe catalyst particles. Whether a Fe–Al spinel forms under catalytic conditions will be a subject of a future investigation.

3.B.b Faceting induced by metals; other adsorbates. Many faceting studies of bimetallic systems have been summarized in review articles.[8,9,16] The motivation for these studies is the thermal stability of bimetallic catalysts. In brief, morphologically-unstable W(111) and Mo(111) coated with a single physical ML of certain metals (Ru, Pd, Rh, Ir, Pt or Au) undergo massive reconstruction from a planar morphology to a microscopically faceted surface upon heating to $T > 700$ K. Annealing is needed to achieve sufficient surface atom mobility for mass transport. Three-sided nanometre-sized pyramids form, in which the facet sides are mainly film-covered {112} faces with pseudomorphic overlayers. Note that a critical coverage, 1 physical ML, is needed to induce faceting by metals (NB: 1 physical ML on W(111) = 3 geometrical MLs = 1.7×10^{15} atoms cm^{-2}. This coverage is needed to completely cover all exposed W atoms on the atomically-rough bcc (111) surfaces).

For most systems studied (Rh, Pd, Ir, Pt and Au on W(111) and W(112)),[50,101,102] a single physical ML (1 ML) of overlayer metal is thermally stable, and "floats" on the outer surface without significant alloy formation for all temperatures up to the onset of desorption. For all systems, except Au/W, multilayer films form alloys upon annealing. Invariably, W atoms from the substrate diffuse into the overlayer film, rather than *vice versa*. In certain cases (Pt/W, Ir/W), evidence for alloy formation in multilayer films is seen from SXPS measurements of sharp 4f levels of both the overlayer and substrate. In general, the alloying behavior of the bimetallic systems is consistent with the known bulk phase diagrams (*e.g.*, Pt is not soluble in W, but W is soluble in Pt to a maximum of ~60% W).

Che *et al.* performed first principles DFT calculations to provide a rationale for the metal-induced faceting of W(111) and Mo(111) in terms of the homogeneous nucleation and growth of facets, driven by the minimization of surface free energy.[26,29] It has been seen experimentally[9,16] that metals having the highest heats of adsorption (*e.g.*, Pt and Pd) and the highest W-4f interfacial binding energies are those that cause faceting.[103] This is consistent with theory, which indicates that a higher heat of adsorption provides both a strong thermodynamic driving force for faceting and a lowered kinetic barrier to faceting.[26,29] An early attempt to correlate faceting with the electronegativity of the overlayer provided a useful guide,[9] but was not supported by theory. A few examples of metal-induced faceting are discussed in more detail in the following paragraphs.

Nucleation and growth during the faceting of a platinum-covered W(111) surface. A combination of powerful microscopic methods, including STM, LEEM and GISAXS, have provided new insights into the mechanism of the metal film-induced faceting of bcc (111) surfaces.[44,104] An STM image of fully-faceted Pt/W(111) is shown in Fig. 14.[44] The Pt coverage is ~1.1 physical ML, and the surface has been annealed to 1100 K.

LEEM can distinguish between planar and faceted surfaces, based on the different diffraction characteristics of low energy electrons on surfaces with different morphologies, with up to ~70 Å lateral resolution. When Pt is dosed from a thermal evaporation source onto the heated surface (~1050 K), the transition from a planar structure to a faceted structure proceeds through the nucleation and growth of spatially separated faceted regions, as shown by LEEM (Fig. 15). The surface remains planar for Pt coverages of less than two-thirds physical ML (1 ML = 1.7×10^{15} atoms cm^{-2}). As the Pt coverage increases above $\frac{2}{3}$ ML on the heated W surface, local islands of Pt, with a coverage of 1 ML, are able to nucleate, and it is there that facets form. When the entire surface is covered by 1 ML, the surface is fully faceted. The STM data of Pelhos *et al.*[44] confirm the LEEM observations that a partially

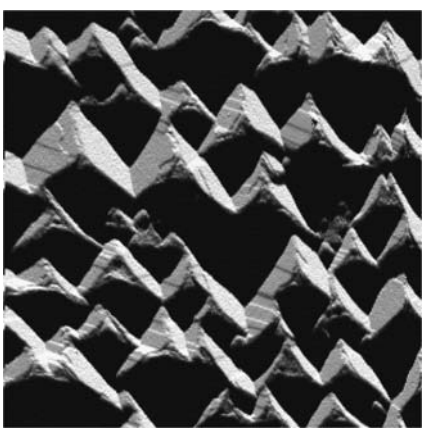

Fig. 14 STM image (200 × 200 nm) of a fully faceted W(111) surface prepared by depositing ~1.1 physical ML Pt and annealed at 1200 K for 1 min. Reproduced with permission from ref. 44 (Copyright 1999, World Scientific).

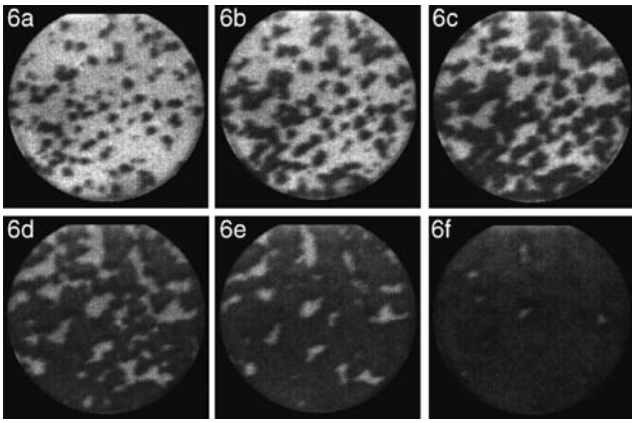

Fig. 15 Bright field LEEM images of the nucleation and growth of faceted regions on Pt/W(111) at a constant temperature ($\sim$1050 K) and Pt flux. The dosing times are 63, 69, 75, 81, 87 and 93 min for images (a)–(f), respectively; $\sim$90 min corresponds to the deposition of 1 physical ML (1.7×10^{15} atom cm^{-2}). The field of view is $\sim$5 mm and the incident electron energy is 5.5 eV. Reprinted from ref. 104 with permission from Elsevier.

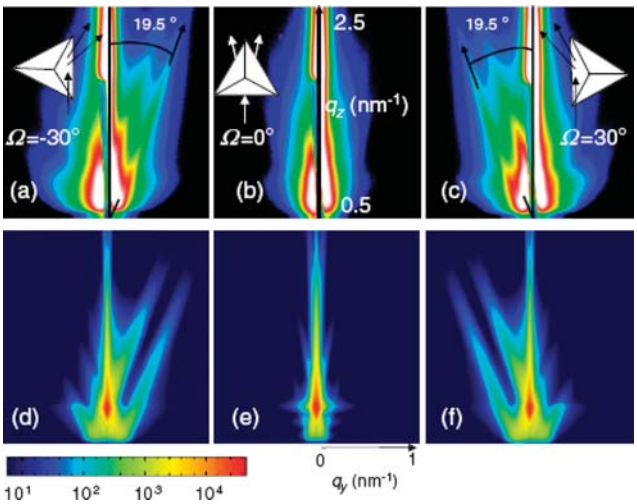

Fig. 16 2-D GISAXS intensity for a faceted Pt/W(211) sample annealed at 1340 K and measured at different azimuth angles. (a)–(c) Experimental GISAXS patterns and (d)–(f) their respective simulated GISAXS patterns. The intensity scale (counts pixel^{-1}) is logarithmic. Reprinted from ref. 54 with permission from Elsevier.

faceted surface is a combination of large planar regions with scattered faceted regions. LEEM and STM prove to be excellent complementary microscopic techniques in the study of faceting.

Additional insights into the Pt-induced faceting of W(111) are provided by the recent X-ray scattering studies of Revenant *et al.*[54] The use of X-rays enables the faceting to be characterized *in situ*, averaged over the whole surface in an ultra-high vacuum (UHV) and in a non destructive way, from very small to very large three-sided pyramids. Morphological and structural features are derived in a combined way from grazing incidence X-ray scattering at small and large emergence angles. Grazing incidence X-ray diffraction (GIXD) probes the order at the atomic scale, while grazing incidence small angle X-ray scattering (GISAXS) probes the morphology and spatial distribution of nanometre-sized objects. Compared to direct imaging techniques, GISAXS offers a high statistical relevance, due to the average over the beam footprint. GISAXS measurements, made as a function of the azimuthal angle Ω (see Fig. 16), unambiguously reveal the three-fold symmetry of the faceting. The data of Fig. 16 were measured at three different values of Ω (0, +30 and −30 degrees). The scattering patterns changed systematically with Ω, as also verified in the simulations of Fig. 16.

The faceting of Pd/W(111). Fig. 17 shows an atomic resolution image of faceted structures in the Pd/W(111) system. For a Pd coverage of $\sim$1.5 ML, annealing at 1075 K transforms the surface into a completely faceted condition. The most remarkable features in this image by Nien and Madey[105] are the atomic row-and-trough structures on individual facets, consistent with their {211} orientation, identified by LEED. The blurred features are identified as disordered Pd overlayers, with local Pd coverage $>$1 ML. The existence of a physical ML of Pd, which covers the W(111) surface without alloy formation in the temperature range of facet formation,

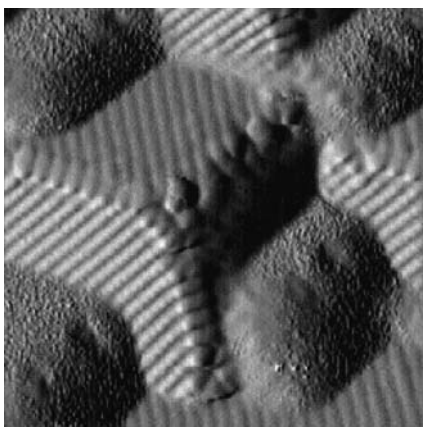

Fig. 17 Atomic resolution STM image (10 × 10 nm) of Pd-covered faceted W(111), prepared by depositing $\sim$1.2 ML Pd and annealing at 1075 K. Reprinted from ref. 105 with permission from Elsevier.

was verified using both low energy ion scattering (LEIS)[106] and soft X-ray photoelectron spectroscopy (SXPS).[50]

3.C Surface chemistry over faceted substrates

Faceted surfaces provide an opportunity to search for nanoscale effects in surface reactions, and to characterize structure-sensitive reactions, *i.e.*, reactions whose rates depend on the local atomic structure of the substrate. Since facets can be grown and destroyed reversibly and facet sizes depend on the annealing temperature, one crystalline sample can be used to prepare multiple substrates, either planar or faceted, with different size distributions. Evidence of structure sensitivity has been seen in *n*-butane hydrogenolysis on planar and faceted Pt/W(111) surfaces,[63] acetylene reactions over bimetallic Pd/W surfaces[58] and methanol reactions over O-modified Re surfaces.[52]

Studies of planar and faceted Ir surfaces have proven especially fruitful. As discussed above, annealing O-covered Ir(210) generates nanoscale pyramids with {311} and (110) facet orientations (see Fig. 3(b)). The average pyramid sizes, 5 to 14 nm, are controlled by the annealing temperature. As illustrated schematically in Fig. 4, oxygen can be completely removed at low T (by exposing to H_2 at 400 K to form H_2O), thus creating a clean faceted surface that is stable up to 600 K. Faceted Ir is a template for studies of many surface reactions whose rates are sensitive to atomic structure and/or nanoscale (facet) size. These include the decomposition of H_2 and NH_3,[46] CO oxidation,[35] the decomposition of acetylene[47] and NO decomposition,[107] as well as other reactions with implications for catalysis. Selected results for the surface chemistry of these model nanoscale catalysts are discussed below.

H_2 and NH_3 decomposition on Ir. The adsorption and decomposition of hydrogen (H_2) and ammonia (NH_3) on clean planar Ir(210) and clean nanoscale-faceted Ir(210) have been characterized using TPD (see Fig. 18 and Fig. 19).[46] Evidence has been seen for structure sensitivity in the recombination and desorption of H_2, and in the thermal decomposition of NH_3 on clean planar Ir(210) *vs.* clean faceted Ir(210).[46] In Fig. 18, the H_2 peak at 360 K, A, is attributed to H_2 desorption from the (110) faces and the H_2 peak at 440 K, B, to the {311} faces of faceted Ir(210).[46] As seen in Fig. 19, both Ir surfaces are highly active toward NH_3 decomposition, and the nitrogen (N_2) desorption peak temperature ($\sim$500 K) is much lower compared to that of other transition metals, suggesting that self-poisoning by N is less of a problem on Ir than on other metal surfaces. Moreover, the decomposition kinetics of NH_3 on faceted Ir(210) exhibit size effects on the nanometre-scale, as evidenced by the changes in the H_2 spectra profiles and the N_2 desorption peak temperature (see Fig. 19).[46] This is the first observation of size effects in surface chemistry on an unsupported monometallic catalyst with a well-defined structure and a controlled size. Our data indicate that iridium is a promising catalyst component for the CO_x-free production of H_2 for fuel cell applications. Faceted Ir(210) is an excellent model nanocatalyst for exploring size effects in surface chemistry.

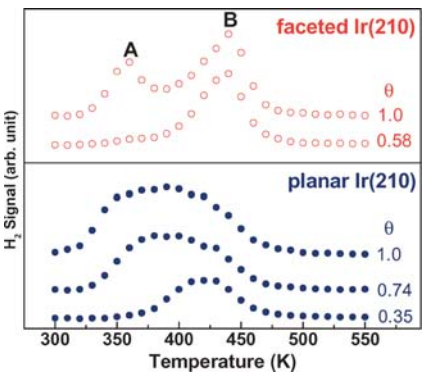

Fig. 18 TPD spectra of H_2 from clean planar Ir(210) and clean faceted Ir(210) (with an average facet size of 14 nm) following adsorption at 300 K. The sample heating rate is $\sim$5 K s^{-1}. Coverages are expressed as a fraction of the saturation coverage at 300 K. Reprinted with permission from ref. 46. Copyright (2005) American Chemical Society.

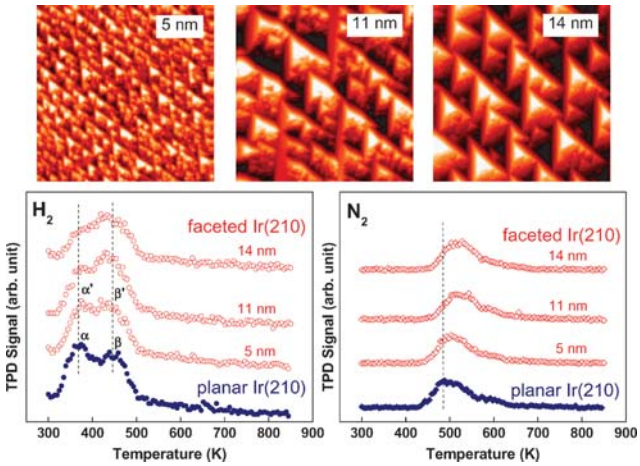

Fig. 19 Top: STM images (100 × 100 nm) of O-covered faceted Ir(210), with different average facet sizes ranging from 5 to 14 nm. Reprinted from ref. 122 with permission from the author and ProQuest LLC. Bottom: TPD spectra of H_2 and N_2 from clean planar Ir(210) and clean faceted Ir(210) with different facet sizes, following adsorption of 5.0 L of NH_3 at 300 K. Reprinted with permission from ref. 46. Copyright (2005) American Chemical Society.

CO oxidation on Ir. In model studies of CO oxidation on O-covered Ir surfaces, we have found evidence for structure sensitivity in CO oxidation on planar *vs.* faceted Ir(210).[35] As shown in Fig. 20, the onset CO_2 desorption temperature is 100 K lower on planar Ir(210) than it is on faceted Ir(210) at low oxygen coverage ($\leq$0.3 ML O), while the temperature for complete CO_2 desorption is 50 K lower on planar Ir(210) than it is on faceted Ir(210) at both low and high oxygen coverages. This indicates that planar Ir(210) is more active than faceted Ir(210) for CO oxidation. Our DFT calculations have revealed that there is a low barrier for 1-D diffusion of O on planar Ir(210) at low oxygen coverage. This unusual 1-D oxygen diffusion may be the key to the higher reactivity of planar Ir(210) for CO oxidation.[108]

NO decomposition on Ir. Both clean planar Ir(210) and clean faceted Ir(210) surfaces are very active for NO decomposition, with a high selectivity to N_2.[107] There is clear evidence for structure sensitivity in NO decomposition on planar *vs.* faceted Ir(210).[107] In particular, no formation of N_2O or NO_2 are observed from faceted Ir(210), while traces of N_2O are formed on planar Ir(210).[107] Moreover, when planar and faceted Ir(210) are pre-covered with up to 0.5 ML O, they

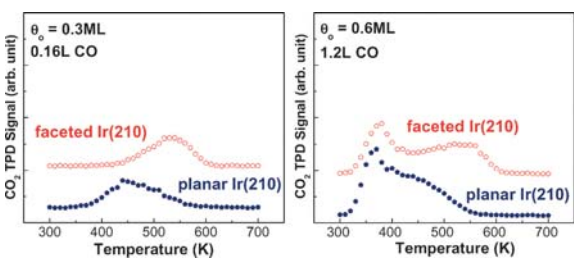

Fig. 20 TPD spectra of CO_2 following the adsorption of CO on O-covered planar and faceted Ir(210), with an average facet size of 14 nm. Reprinted with permission from ref. 35. Copyright (2006) American Chemical Society.

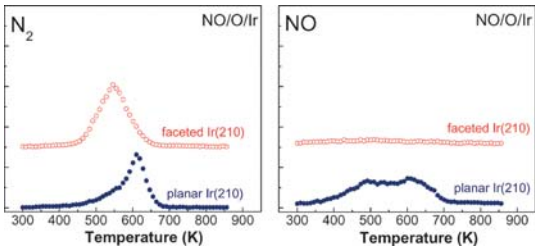

Fig. 21 TPD spectra of N-containing species from planar and faceted Ir(210), obtained by exposing them first to O_2 and then to ^{15}NO at 300 K. The average facet size of faceted Ir(210) is $\sim$14 nm.[107]

continue to exhibit an unexpectedly high reactivity for NO decomposition.[107] For higher O coverages (0.7 ML O), faceted Ir(210) is much more active than planar Ir(210) for NO decomposition, as shown in Fig. 21,[107] indicating a strong structure sensitivity in NO decomposition. The reactivity of planar and faceted Ir(210), especially the high reactivity of faceted Ir(210) for NO decomposition in the presence of high oxygen pre-coverage, are surprising findings, which may be of importance for the development of Ir-based catalysts for NO decomposition in current diesel and lean-burn engines, which operate under high oxygen concentrations that poison most Pt-based catalysts.

Concluding this section, we note that it is not possible to remove ambiguities completely in complex catalytic studies over faceted single-crystal surfaces. However, we suggest that this approach is an important step in trying to determine structure/reactivity relationships in metallic systems. One can take advantage of the morphological instability of atomically-rough transition metal substrates to create novel metallic catalyst surfaces. It is important to determine whether or not there are substantial differences in the selectivity and activity of the different surfaces before one can address in detail the atomistic mechanisms.

3.D Faceting of semiconductors and oxides

While adsorbed layers are required to cause substantial faceting of clean planar metal surfaces, there are many examples in which faceting of atomically clean semiconductor and oxide surfaces are observed. In these cases, there is sufficient anisotropy in surface free energy that unstable surfaces in certain crystallographic directions spontaneously reconstruct to form faceted structures upon annealing.

Faceting of Si, Ge and GaAs. Williams and Bartelt[109] used statistical mechanical models to describe their experimental observation of the faceting of stepped (vicinal) Si surfaces. They observed that profound changes in surface morphology occurred when steps coalesced to form facets. That is, step-bunching upon annealing vicinal surfaces lead to the growth of both terraces and multi-atom-high faceted steps (see Fig. 22).[109] Step-bunching has also been reported for vicinal GaAs (100) surfaces (see ref. 20 and citations therein).

Gai *et al.*[110,111] have carried out extensive studies on the thermal stability of Si and Ge surfaces. They concluded for Ge that there are 14 stable surfaces and that all other surfaces are unstable. Upon annealing to a sufficiently high temperature, all other surfaces developed facets of one or more of the

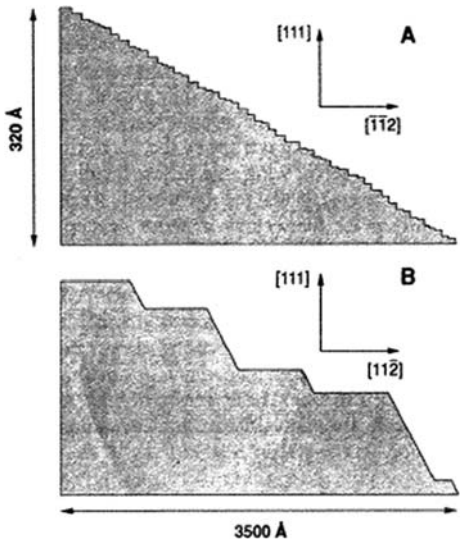

Fig. 22 Surface profiles of two silicon surfaces, each mis-oriented from the (111) direction by 4°, but along different azimuthal directions (1, 2). A: Mis-orientation azimuth [$\bar{1}\bar{1}$2] and B: mis-orientation azimuth [11$\bar{2}$]. Data were compiled by "tiling" adjacent atomic resolution STM scans to form a composite profile covering a cross section 4000 Å wide. From ref. 109. Reprinted with permission from AAAS.

14 stable surfaces. Moreover, seven of the fourteen were major stable surfaces (MAJOR), while the rest were minor stable surfaces (MINOR). The distinction between MAJOR and MINOR is that the unit cell of any MINOR surface is faceted to the nanofacets of one or more MAJOR. Similar behavior was observed for surfaces of Si. Fig. 23 shows unit stereographic triangles of Ge and Si, indicating the stable MAJOR and MINOR surfaces for each.[110]

Faceting of oxide surfaces. The stability of polar oxide surfaces has been studied using electron microscopy by Gajdardziska-Josifovska *et al.*[112,113] They focused on surfaces with the rock salt structure, MgO and NiO, and showed that vacuum annealing lead to striking faceted reconstructions in the polar (111) surfaces. Their careful work settled a long-term controversy concerning the orientations of thermally-induced facets on MgO(111).

We have already seen in Fig. 1 (above) that rutile TiO_2 nanoparticles exhibit well-defined facets. The planar rutile TiO_2(100) surface has been reported to develop nanofacets in the annealed (1 × 3) structure, but this is still a matter of some controversy.[114] However, recent studies of low-dimensional reduced phases of ultrathin TiO_2 films grown on Ni(110) substrates show beautifully-developed facets with dimensions $\sim$100 nm. The facets are interpreted as being a consequence of crystallographic shearing of the reduced thin films (see Fig. 24).[115]

3.E The use of faceted surfaces as nanotemplates for preferential nucleation

An unusual aspect of faceted surfaces has begun to be explored in recent years, *i.e.*, the use of faceted substrates as self-assembled nanotemplates for a variety of applications.

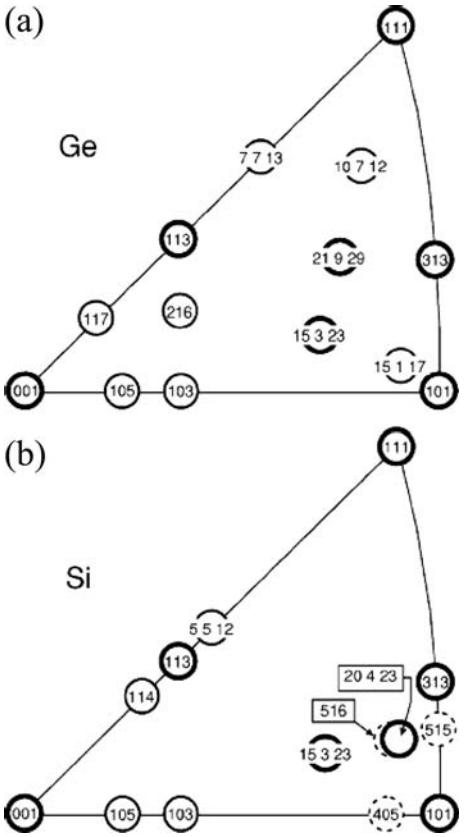

Fig. 23 (a) Unit stereographic triangle of germanium, showing all seven major stable surfaces (MAJOR, thick circles) and all seven minor stable surfaces (MINOR, thin circles). (b) Unit stereographic triangle for silicon, showing the MAJORs and MINORs found so far, as well as the three unstable surfaces (dotted circles): (515), (516) and (405). Reprinted with permission from ref. 110. Copyright (2001) by the American Physical Society. URL: http://link.aps.org/abstract/PRB/v64/e125201.

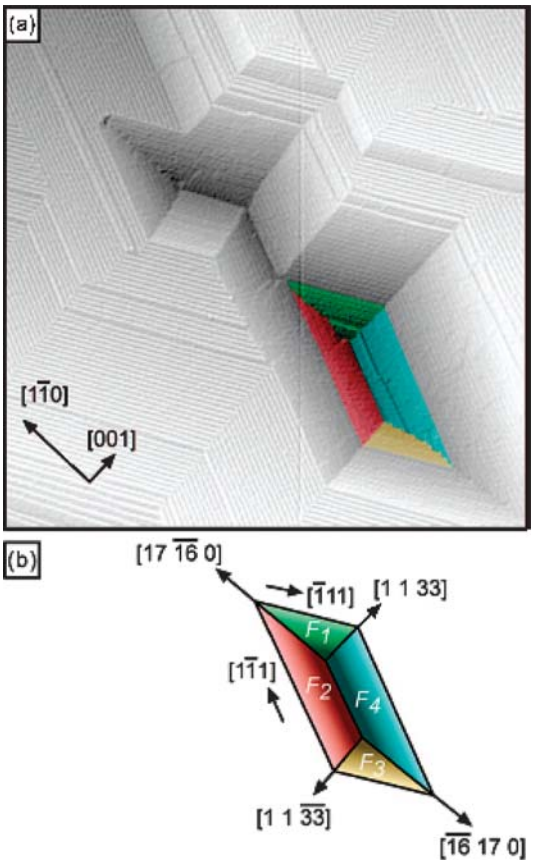

Fig. 24 (a) Differentiated STM image of a crystallographically-sheared TiO_2 film (360 × 360 nm, 0.50 V, 4.82 nA). The arrows indicate the principal azimuths of the TiO_2(110) surface. Parts of four facets are highlighted by different colors. (b) Schematic representation of the facet arrangement in the lower part of the STM image, using the same color coding as in (a). *F1*, *F2*, *F3* and *F4* correspond to the (16 17 $\bar{1}$), (16 17 1), (17 16 1) and (17 16 $\bar{1}$) planes, respectively. The arrows indicate intersections of the facets with each other, and with the (110) plane. Reprinted with permission from ref. 115. Copyright (2007) American Chemical Society.

These include the self-assembly of nanowires or other metallic nanostructures, highly selective supported catalysts or masters for making stamps used in the patterning of biosensors on surfaces. Some representative examples are given below.

Faceted Re as a nanotemplate for metal particle growth. The achievement of a high degree of selectivity in heterogeneous catalysis continues to be a major scientific and technical challenge. There is strong evidence that the geometrical and electronic structure of nanometre-scale supported catalyst particles play a major role in selectivity. One goal for faceted nanotemplate surfaces is to identify substrates and processes that may allow nucleation at specific sites of supported metal catalysts, with narrow size distributions and regular spacings on the nanometre-scale. The potential benefit is synthesis of active model catalysts with high selectivity.

As a model system, O-covered nanofaceted Re(12$\bar{3}$1) has been used as a nanotemplate substrate for the growth of Co particles in 1-D arrays from vapor deposited Co (see Fig. 7). Co was chosen for its potential catalytic and magnetic applications, and the results could be compared with the Co/Pt/W(111) system, where Co nanoclusters in a registry with Pt/W pyramidal facets were observed.[54] The initial results showed

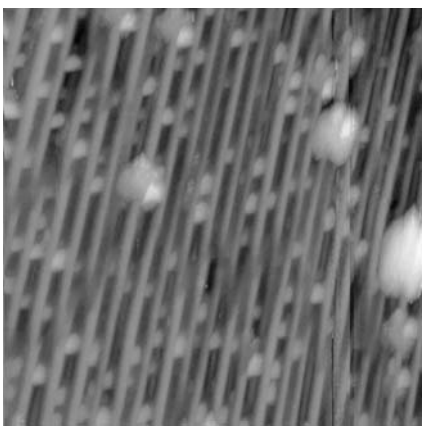

Fig. 25 An STM image (350 × 350 nm) showing 1-D arrays of Co clusters on a faceted O/Re(12$\bar{3}$1) surface. The surface was prepared by depositing 2 ML Co on an O-saturated faceted Re(12$\bar{3}$1) surface at 300 K, followed by annealing at 800 K.[36]

great promise, as Co nanoparticles nucleated selectively in the troughs (Fig. 25).[36,116] No evidence was found for nucleation outside the troughs, *e.g.* atop the ridges. This observation has important implications for the preparation of model supported catalysts with a narrow size distribution, and is being extended to other systems of greater catalytic interest.

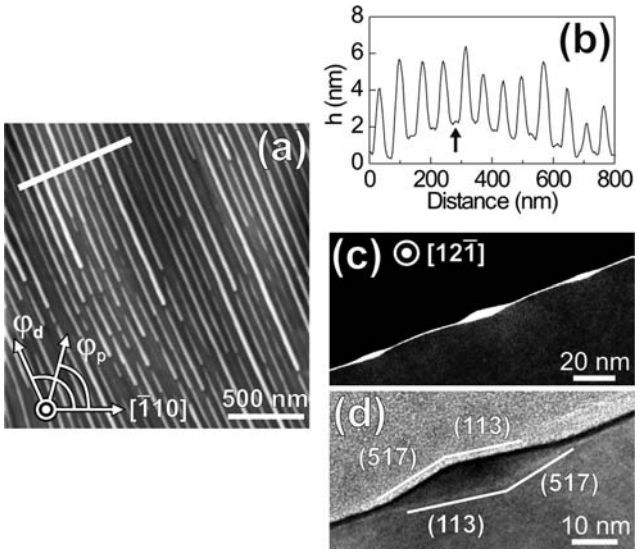

Fig. 26 Self-organized Ge nanowires formed on Si(173 100 373), corresponding to an azimuthal direction $\varphi_p = 75°$ with $\theta = 28.2°$. (a) AFM image with a scan size of $2.0 \times 2.0\ \mu m^2$. (b) Height h as a function of the position along the white line in (a). (c) Z-contrast STEM image of the Ge nanowires shown in (a). (d) High-resolution [12$\bar{1}$] zone-axis XTEM image. Reprinted with permission from ref. 117. Copyright (2005) American Chemical Society.

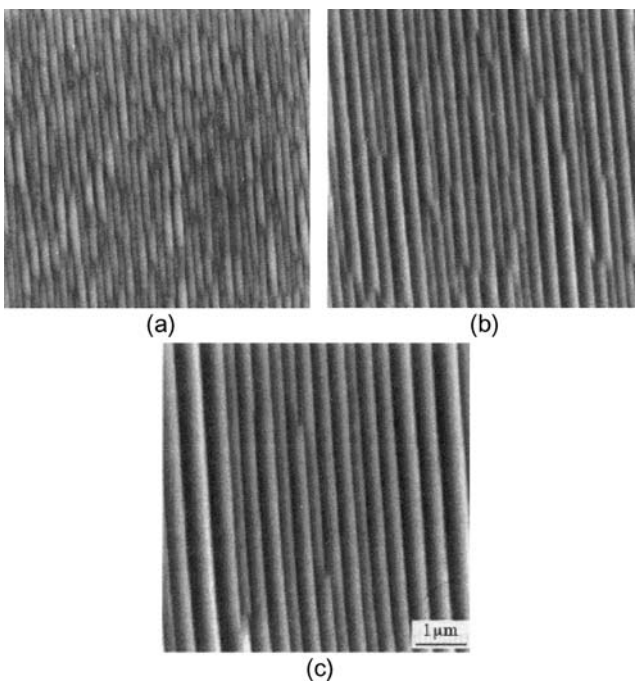

Fig. 27 AFM images of the $\{10\bar{1}0\}$ Al_2O_3 surface. These substrates have been annealed at 1400 °C for different lengths of time: (a) 4 h, (b) 6 h and (c) 12 h. The images show the increase in the facet wavelength and the decrease in the density of facet junctions. Reprinted from ref. 59 with permission from Elsevier.

Faceted Si as a nanotemplate. The work of Gai *et al.*[110] on the faceting of Si surfaces is described in section 3.D. They suggested that certain crystallographic orientations of Si, after annealing at an elevated temperature, may be used as nanotemplates with a variable cross-section to grow "quantum wires" and other nanostructures. Ohmori *et al.*[117] developed this idea (Fig. 26) and showed that Ge nanowires could be grown on an annealed Si(173 100 373) surface that had a hill-and-valley structure, consisting of alternating (113) and (517) facets (note that (113) is classified as a MAJOR facet according to Gai *et al.*;[110] see Fig. 23 above and related discussion).

The faceting of oxide surfaces by heating in air: nanofacet lithography. Whereas all the faceting studies described up to

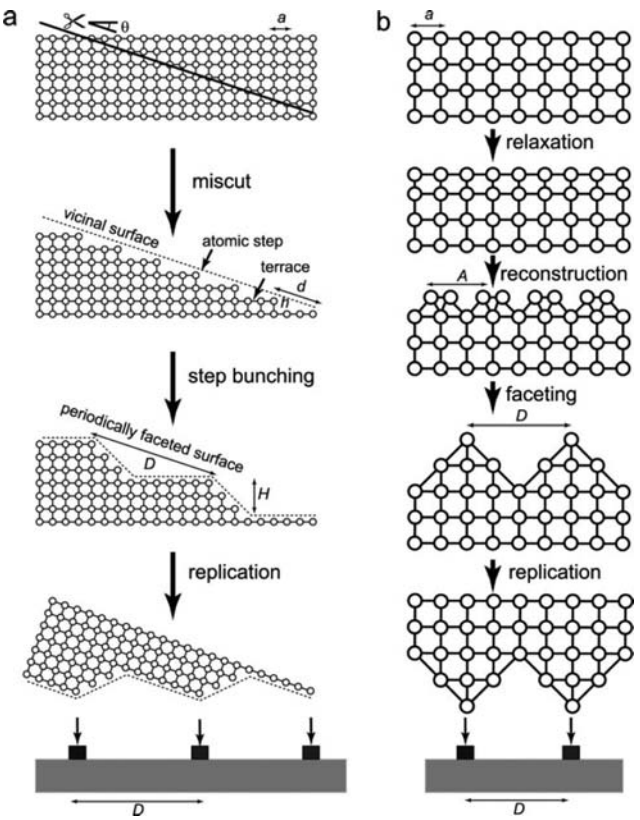

Fig. 28 Schematic representations of the "Nanofacet Lithography" approach: different self-structuring processes at (a) vicinal (*e.g.*, stepped α-$Al_2O_3(0001)$) and (b) singular (*e.g.*, $Al_2O_3(10\bar{1}0)$) crystal surfaces, leading to increases in the period and their subsequent replication to other media: (a) a mis-cut by an angle θ increases the surface pitch from a to d, with feature height h; step-bunching further increases the pitch to D, with feature height H. (b) The relaxation and reconstruction of $(10\bar{1}0)$ increases the surface pitch from a to A, and faceting further increases the pitch to D, with a feature height of the same order of magnitude. Figure and caption from Gabai *et al.* Reproduced from ref. 119 with permission. Copyright (2007) Wiley-VCH Verlag GmbH & Co. KGaA.

this point have been carried out under vacuum conditions, there have been reports recently that certain oxide surfaces develop facets upon annealing to elevated temperatures in air, or in gas mixtures at atmospheric pressure. The motivation is the development of templates for the deposition of metallic nanostructures, or the use of faceted substrates as masters for making ''stamps'' for the patterning of biomolecular sensors onto substrates.

Several groups have reported the faceting of Al_2O_3 surfaces following heating in air from 1100 to 1500 °C.[55,59,118,119] Heffelfinger *et al.*[59,118] and Huth *et al.*[55] found that the planar M-plane sapphire ($10\bar{1}0$) surface was unstable upon annealing in air and spontaneously formed long ridge-like structures, primarily with ($1\bar{1}01$) and ($1\bar{1}02$) nanofacets. Upon heating in air at 1400 °C, individual facets nucleated and initially grew. After 4 h at 1400 °C, the surface was faceted into a complete hill-and-valley structure, whose facet wavelength increased with further annealing (see Fig. 27).[59] Gabai *et al.*[119] confirmed that unstable M-plane sapphire develops ridge-like facets, with peaks and V-shaped grooves. In contrast, vicinal mis-cut C-plane sapphire, *i.e.* vicinal alpha alumina (0001) tilted by 2° toward [$1\bar{1}00$], develops nanosteps, consistent with step-bunching.

A schematic of the distinction between the step-bunching of a vicinal Al_2O_3 surface and the faceting reconstruction of a low-index surface, such as ($10\bar{1}0$), is shown in Fig. 28.[119] This figure also illustrates the use of the faceted surface as a potential ''stamp'' for replication, in the approach Gabai *et al.* call ''Nanofacet Lithography'' (NFL).[119] A more detailed flowchart, showing the creation of cast PDMS stamps using nanofaceted Al_2O_3 as a ''master'', is shown in Fig. 29.[119]

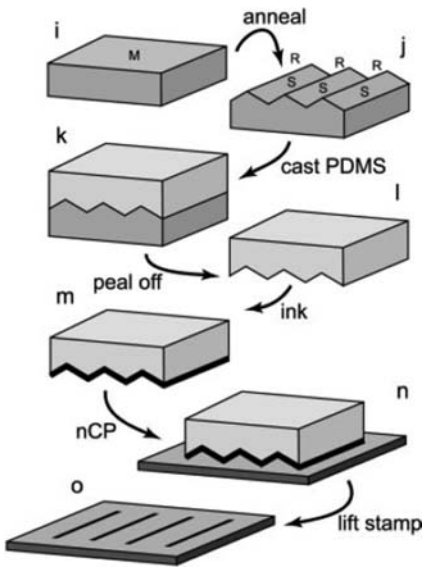

Fig. 29 Flowchart describing the processes of ''Nanofacet Lithography'' using singular M-plane sapphire. (i) A cut along the M-plane produces an unstable surface of singular α-Al_2O_3 ($10\bar{1}0$). (j) Annealing leads to S-/R-faceted, V-shaped nanogrooves. (k) Cast PDMS. (l) Peal-off PDMS stamp. (m) Ink PDMS stamp in a solution of thiol or silane. (n) Nanocontact printing (nCP) on a target surface of Au and Si/SiO_2, respectively. (o) Lift stamp. Reproduced from ref. 119 with permission. Copyright (2007) Wiley-VCH Verlag GmbH & Co. KGaA.

Such stamps can be used in nanoimprint lithography to deposit periodic arrays of self-assembled alkane-thiol MLs, or even biofunctionalized nanoarrays comprising of different proteins.[120]

Faceted Al_2O_3 surfaces have also been explored as substrates for the growth of nanowires and nanostripe arrays. Huth *et al.*[55] used nanofaceted $Al_2O_3(10\bar{1}0)$ as a substrate for the MBE (molecular beam epitaxy) growth of Fe and Nb at controlled, shallow incidence angles, which lead to geometrical ''shadowing'' by the nanofacets. Spatially-separated 100 nm-wide Nb nanostripes were demonstrated.

Benedetti *et al.*[121] have shown that nanofaceting is not limited to Al_2O_3 heated in air. They prepared stepped MgO surfaces mis-cut from the stable (100) cleavage plane by 2° and 6°. Upon heating to ~1000 °C for 1 to 6 h in a 50/50 mixture of O_2 and N_2, they found that the surfaces developed regular arrays of steps, whose morphology depended on the annealing time and temperature.[121] Faceting was attributed to a step-bunching mechanism (large terraces connected by multiple atom height steps) similar to that shown in Fig. 28a.

4. Summary: perspective

This review focused on new aspects of nanoscale phenomena in surface chemistry. Our aim was to characterize the physics and chemistry of facet nucleation and growth on a variety of metal, semiconductor and oxide surfaces. Faceting is generally driven by thermodynamics (the minimization of surface free energy) but limited by kinetics (surface diffusion, nucleation and growth). Although clean, planar metal surfaces do not generally develop facets spontaneously, adsorbed MLs can affect the anisotropy of the surface free energy and create conditions favorable for faceting. Faceting is often observed for atomically-rough surfaces that become morphologically unstable when covered by adsorbed gases and annealed. First principles theory has been compared to experiment, providing useful insights into the stability of various surfaces.

We also examined the relationships between nanometre-scale surface features and heterogeneous catalytic chemistry in a number of simple reactions. A unique characteristic of these studies of model catalysts was our emphasis on atomically-rough, high surface energy surfaces that were morphologically unstable under the reaction conditions used. The results will help our understanding of dynamic structural rearrangements at the surfaces of high area supported catalysts, and in clarifying the role of nanometre-scale size effects in surface reactions.

Finally, we discussed the use of faceted surfaces as self-assembled nanotemplates, with interesting potential applications such as the synthesis of model supported catalysts (metals on oxides), substrates for the growth of nanowires and nanofacet lithography (including the patterning of organic self-assembled monolayers and the deposition of nanoarrays of biomolecules). The applications of faceted surfaces in nanotechnology—especially surfaces faceted by heating in air—are certain to blossom in the coming years.

Acknowledgements

The Rutgers authors acknowledge the support of the US Department of Energy, Office of Basic Energy Sciences during

the course of this work. We also thank the many Rutgers graduate students and postdocs, whose work through the years has contributed to our understanding of faceting phenomena: I. Abdelrehim, R. Baier, R. Barnes, S. Brown, R. A. Campbell, A. S. Y. Chan, C.-Z. Dong, I. Ermanoski, M. Gladys, Govind, J. Guan, G. Jackson, N. M. Jisrawi, J. J. Kolodziej, E. Loginova, C.-H. Nien, K. Pelhos, J. Quinton, M. Reyhan, Q. Shen, K. J. Song, H. S. Tao and Q. Wu. The FHI and Ulm authors acknowledge support by the Fonds der Chemischen Industrie (FCI), the Deutscher Akademischer Austauschdienst (DAAD) and the Deutsche Forschungsgemeinschaft (DFG) within the Emmy Noether Program.

References

1 C. Herring, in *Structure and Properties of Solid Surfaces*, ed. R. Gomer and C. S. Smith, University of Chicago Press, Chicago, 1953, pp. 5–72.
2 J. M. Blakely and M. Eizenberg, in *The Chemical Physics of Solid Surfaces and Heterogeneous Catalysis*, ed. D. A. King and D. P. Woodruff, Elsevier, Amsterdam, 1981, vol. I, pp. 1–80.
3 M. Flytzani-Stephanopoulos and L. D. Schmidt, *Prog. Surf. Sci.*, 1979, **9**, 83–111.
4 C. R. Henry, *Surf. Sci. Rep.*, 1998, **31**, 231–325.
5 A. K. Datye and D. J. Smith, *Catal. Rev. Sci. Eng.*, 1992, **34**, 129–178.
6 T. Ohno, K. Sarukawa and M. Matsumura, *New J. Chem.*, 2002, **26**, 1167–1170.
7 M. Ramamoorthy, D. Vanderbilt and R. D. King-Smith, *Phys. Rev. B: Condens. Matter Mater. Phys.*, 1994, **49**, 16721–16727.
8 T. E. Madey, K. Pelhos, Q. Wu, R. Barnes, I. Ermanoski, W. Chen, J. J. Kolodziej and J. E. Rowe, *Proc. Natl. Acad. Sci. U. S. A.*, 2002, **99**, 6503–6508.
9 T. E. Madey, J. Guan, C. H. Nien, C. Z. Dong, H. S. Tao and R. A. Campbell, *Surf. Rev. Lett.*, 1996, **3**, 1315–1328.
10 G. A. Somorjai and Y. G. Borodko, *Catal. Lett.*, 2001, **76**, 1–5.
11 G. A. Somorjai, *Introduction to Surface Chemistry and Catalysis*, Wiley-Interscience, New York, 1994.
12 G. A. Somorjai, R. L. York, D. Butcher and J. Y. Park, *Phys. Chem. Chem. Phys.*, 2007, **9**, 3500–3513.
13 H. Fornander, L.-G. Ekedahl and H. Dannetun, *Surf. Sci.*, 1999, **441**, 479–492.
14 H. Lee, S. E. Habas, S. Kweskin, D. Butcher, G. A. Somorjai and P. Yang, *Angew. Chem., Int. Ed.*, 2006, **45**, 7824–7828.
15 E. V. Shevchenko, D. V. Talapin, N. A. Kotov, S. Obrien and C. B. Murray, *Nature*, 2006, **439**, 55–59.
16 T. E. Madey, C. H. Nien, K. Pelhos, J. J. Kolodziej, I. M. Abdelrehim and H. S. Tao, *Surf. Sci.*, 1999, **438**, 191–206.
17 E. D. Williams and N. C. Bartelt, in *Handbook of Surface Science*, ed. W. N. Unertl, Elsevier, Amsterdam, 1996, ch. 2, pp. 51–99.
18 Q. Chen and N. V. Richardson, *Prog. Surf. Sci.*, 2003, **73**, 59–77.
19 E. Bauer, in *The Chemical Physics of Solid Surfaces and Heterogeneous Catalysis*, ed. D. A. King and D. P. Woodruff, Elsevier, Amsterdam, 1984, vol. III B, pp. 1–57.
20 V. A. Shchukin and D. Bimberg, *Rev. Mod. Phys.*, 1999, **71**, 1125–1171.
21 H. v. Beijeren, *Phys. Rev. Lett.*, 1977, **38**, 993–996.
22 S. Prestipino, G. Santoro and E. Tosatti, *Phys. Rev. Lett.*, 1995, **75**, 4468–4471.
23 G. Mazzeo, E. Carlon and H. v. Beijeren, *Phys. Rev. Lett.*, 1995, **74**, 1391–1394.
24 V. P. Zhdanov and B. Kasemo, *Phys. Rev. B: Condens. Matter Mater. Phys.*, 1997, **56**, R10067–R10070.
25 C. Oleksy, *Surf. Sci.*, 2004, **549**, 246–254.
26 J. G. Che, C. T. Chan, C. H. Kuo and T. C. Leung, *Phys. Rev. Lett.*, 1997, **79**, 4230–4233.
27 C. T. Chan, J. G. Che and T. C. Leung, *Prog. Surf. Sci.*, 1998, **59**, 1–11.
28 J. G. Che and C. T. Chan, *Surf. Sci.*, 1998, **401**, L432–L436.
29 C. H. Nien, T. E. Madey, Y. W. Tai, T. C. Leung, J. G. Che and C. T. Chan, *Phys. Rev. B: Condens. Matter Mater. Phys.*, 1999, **59**, 10335–10340.
30 P. Kaghazchi, T. Jacob, I. Ermanoski, W. Chen and T. E. Madey, *ACS Nano*, 2008, **2**, 1280–1288.
31 P. Kaghazchi and T. Jacob, *Phys. Rev. B: Condens. Matter Mater. Phys.*, 2007, **76**, 245425.
32 K.-J. Song, J. C. Lin, M. Y. Lai and Y. L. Wang, *Surf. Sci.*, 1995, **327**, 17–32.
33 K.-J. Song, W.-R. Chen, V. Yeh, Y.-W. Liao, P. T. Tsao and M.-T. Lin, *Surf. Sci.*, 2001, **478**, 145–168.
34 D. B. Dan'ko, M. Kuchowicz, R. Szukiewicz and J. Kolaczkiewicz, *Surf. Sci.*, 2006, **600**, 2258–2267.
35 W. Chen, I. Ermanoski, T. Jacob and T. E. Madey, *Langmuir*, 2006, **22**, 3166–3173.
36 H. Wang, PhD thesis, Rutgers University, 2008.
37 H. Wang, A. S. Y. Chan, W. Chen, P. Kaghazchi, T. Jacob and T. E. Madey, *ACS Nano*, 2007, **1**, 449–455.
38 P. Kaghazchi, K. A. Soliman, F. C. Simeone, L. A. Kibler and T. Jacob, *Faraday Discuss.*, DOI: 10.1039/b802919a.
39 M. Scheffler and J. Dabrowski, *Philos. Mag. A*, 1988, **58**, 107–121.
40 G.-X. Qian, R. M. Martin and D. J. Chadi, *Phys. Rev. B: Condens. Matter Mater. Phys.*, 1988, **38**, 7649–7663.
41 K. Reuter and M. Scheffler, *Phys. Rev. B: Condens. Matter Mater. Phys.*, 2001, **65**, 035406.
42 I. Ermanoski, K. Pelhos, W. Chen, J. S. Quinton and T. E. Madey, *Surf. Sci.*, 2004, **549**, 1–23.
43 H. Wang, W. Chen and T. E. Madey, *Phys. Rev. B: Condens. Matter Mater. Phys.*, 2006, **74**, 205426.
44 K. Pelhos, T. E. Madey, J. B. Hannon and G. L. Kellogg, *Surf. Rev. Lett.*, 1999, **6**, 767–774.
45 I. Ermanoski, W. Swiech and T. E. Madey, *Surf. Sci.*, 2005, **592**, L299–L304.
46 W. Chen, I. Ermanoski and T. E. Madey, *J. Am. Chem. Soc.*, 2005, **127**, 5014–5015.
47 W. Chen, I. Ermanoski, Q. Wu, T. E. Madey, H. H. Hwu and J. G. Chen, *J. Phys. Chem. B*, 2003, **107**, 5231–5242.
48 A. Cetronio and J. P. Jones, *Surf. Sci.*, 1973, **40**, 227–248.
49 A. Szczepkowicz, A. Ciszewski, R. Bryl, C. Oleksy, C. H. Nien, Q. Wu and T. E. Madey, *Surf. Sci.*, 2005, **599**, 55–68.
50 J. J. Kolodziej, T. E. Madey, J. W. Keister and J. E. Rowe, *Phys. Rev. B: Condens. Matter Mater. Phys.*, 2002, **65**, 075413.
51 M. J. Gladys, I. Ermanoski, G. Jackson, J. S. Quinton, J. E. Rowe and T. E. Madey, *J. Electron Spectrosc. Relat. Phenom.*, 2004, **135**, 105–112.
52 A. S. Y. Chan, W. Chen, H. Wang, J. E. Rowe and T. E. Madey, *J. Phys. Chem. B*, 2004, **108**, 14643–14651.
53 E. Loginova and T. E. Madey, unpublished work.
54 C. Revenant, F. Leroy, G. Renaud, R. Lazzari, A. Létoublon and T. Madey, *Surf. Sci.*, 2007, **601**, 3431–3449.
55 M. Huth, K. A. Ritley, J. Oster, H. Dosch and H. Adrian, *Adv. Funct. Mater.*, 2002, **12**, 333–338.
56 L. A. Kibler and T. Jacob, in preparation.
57 M. Sander, R. Imbihl, R. Schuster, J. V. Barth and G. Ertl, *Surf. Sci.*, 1992, **271**, 159–169.
58 R. Barnes, I. M. Abdelrehim and T. E. Madey, *Top. Catal.*, 2001, **14**, 53–61.
59 J. R. Heffelfinger and C. B. Carter, *Surf. Sci.*, 1997, **389**, 188–200.
60 J. Guan, R. A. Campbell and T. E. Madey, *Surf. Sci.*, 1995, **341**, 311–327.
61 C. Z. Dong, S. M. Shivaprasad, K. J. Song and T. E. Madey, *J. Chem. Phys.*, 1993, **99**, 9172–9181.
62 T. E. Madey, J. Guan, C. Z. Dong and S. M. Shivaprasad, *Surf. Sci.*, 1993, **287–288**, 826–830.
63 R. A. Campbell, J. Guan and T. E. Madey, *Catal. Lett.*, 1994, **27**, 273–280.
64 R. E. Cunningham and A. T. Gwathmey, *J. Chim. Phys. Phys.–Chim. Biol.*, 1954, **51**, 497–507.
65 P. L. J. Gunter, J. W. Niemantsverdriet, F. H. Ribeiro and G. A. Somorjai, *Catal. Rev. Sci. Eng.*, 1997, **39**, 77–168.
66 D. Kolthoff, T. Dullweber and H. Pfnur, *Surf. Sci.*, 2000, **447**, 259–271.
67 G. Rupprechter, K. Hayek and H. Hofmeister, *J. Catal.*, 1998, **173**, 409–422.

68 P. J. Knight, S. M. Driver and D. P. Woodruff, *Surf. Sci.*, 1997, **376**, 374–388.
69 S. Reiter and E. Taglauer, *Surf. Sci.*, 1996, **367**, 33–39.
70 E. Taglauer, S. Reiter, A. Liegl and S. Schömann, *Nucl. Instrum. Methods Phys. Res., Sect. B*, 1996, **118**, 456–461.
71 Q. Wu, J. J. Kolodziej, H. Wang and T. E. Madey, unpublished work.
72 F. Bönczek, T. Engel and E. Bauer, *Surf. Sci.*, 1980, **97**, 595–608.
73 J. C. Tracy and J. M. Blakely, *Surf. Sci.*, 1969, **13**, 313–336.
74 H. Niehus, *Surf. Sci.*, 1979, **87**, 561–580.
75 C. Zhang, M. A. Van Hove and G. A. Somorjai, *Surf. Sci.*, 1985, **149**, 326–340.
76 D. R. Strongin and G. A. Somorjai, *J. Catal.*, 1989, **118**, 99–110.
77 J. W. Dickinson, J. C. Moore and A. A. Baski, *Surf. Sci.*, 2004, **561**, 193–199.
78 E. R. Frank and R. J. Hamers, *J. Catal.*, 1977, **172**, 406–413.
79 J. Gustafson, A. Resta, A. Mikkelsen, R. Westerstrom, J. N. Anderson and E. Lundgren, *Phys. Rev. B: Condens. Matter Mater. Phys.*, 2006, **74**, 035401.
80 J. C. W. Tucker, *Acta Metall.*, 1967, **15**, 1465–1474.
81 Govind, W. Chen, H. Wang and T. E. Madey, unpublished work.
82 E. Loginova, F. Cosandey and T. E. Madey, *Surf. Sci.*, 2007, **601**, L11–L14.
83 B. J. McIntyre, M. Salmeron and G. A. Somorjai, *J. Vac. Sci. Technol., A*, 1993, **11**, 1964–1968.
84 R. E. Kirby, C. S. McKee and M. W. Roberts, *Surf. Sci.*, 1976, **55**, 725–728.
85 R. E. Kirby, C. S. McKee and L. V. Renny, *Surf. Sci.*, 1980, **97**, 457–477.
86 K. F. Peters, C. J. Walker, P. Steadman, O. Robacvh, H. Isern and S. Ferrer, *Phys. Rev. Lett.*, 2001, **86**, 5325–5328.
87 V. Johanek, M. Laurin, A. W. Grant, B. Kasemo, C. R. Henry and J. Libuda, *Science*, 2004, **304**, 1639–1644.
88 I. Ermanoski, C. Kim, S. Kelty and T. E. Madey, *Surf. Sci.*, 2005, **596**, 89–97.
89 C. Voss and N. Kruse, *Surf. Sci.*, 1998, **409**, 252–257.
90 All calculations were performed using the CASTEP code (M. D. Segall, P. J. D. Lindan, M. J. Probert, C. J. Pickard, P. J. Hasnip, S. J. Clark and M. C. Payne, *J. Phys.: Condens. Matter*, 2002, **14**, 2717–2744) with a plane-wave basis set (E_{cutoff} = 340 eV), Vanderbilt ultrasoft pseudopotentials (D. Vanderbilt, *Phys. Rev. B: Condens. Matter Mater. Phys.*, 1990, **41**, 7892–7895) and the PBE-GGA exchange correlation functional (J. P. Perdew, K. Burke and M. Ernzerhof, *Phys. Rev. Lett.*, 1996, **77**, 3865–3868). The surfaces were modeled by 16-layer slabs for Ir(210), 11-layer slabs for Ir(311), 12-layer slabs for Ir(110) and 7-layer slabs for the Ir(110)-superstructure, where, during structure optimization, the bottom three to four layers were fixed at the calculated bulk crystal structure. The Brillouin zones of the (1 × 1) surface unit cells of the Ir(210), (311), (110) and (110)-superstructure were sampled with 10 × 8, 14 × 8, 14 × 10 and 4 × 4 Monkhorst-Pack *k*-point meshes, respectively.
91 T. Jacob, P. Kaghazchi, I. Ermanoski, W. Chen and T. E. Madey, unpublished work.
92 Y. Yuan, H. Liu, H. Imoto, T. Shido and Y. Iwasawa, *J. Catal.*, 2000, **195**, 51–61.
93 F. Solymosi, P. Tolmacsov and T. S. Zakar, *J. Catal.*, 2005, **233**, 51–59.
94 K. Liu, S. C. Fung, T. C. Ho and D. S. Rumschitzki, *J. Catal.*, 2002, **206**, 188–201.
95 P. Kaghazchi, T. Jacob, H. Wang and T. E. Madey, to be submitted.
96 The calculations were equivalent to ref. 90, but with E_{cutoff} = 340 eV for all O-adsorbed systems and E_{cutoff} = 380 eV in the case of nitrogen. The slab thicknesses and *k*-point meshes per (1 × 1) surface unit cell were: 19-layers and (4 × 4) for Re(11$\bar{2}$1), 30-layers and (3 × 3) for Re(13$\bar{4}$2)/Re(31$\bar{4}$2), 11-layers and (8 × 5) for Re(10$\bar{1}$0)/Re(01$\bar{1}$0), and finally 14-layers and (8 × 4) for Re(10$\bar{1}$1)/Re(01$\bar{1}$1).
97 H. Wang, W. Chen. P. Kaghazchi, T. Jacob and T. E. Madey, unpublished work.
98 N. J. Taylor, *Surf. Sci.*, 1964, **2**, 544–552.
99 C.-H. Nien, PhD thesis, Rutgers University, 1999.
100 E. Loginova, PhD thesis, Rutgers University, 2008.
101 J. J. Kolodziej, K. Pelhos, I. M. Abdelrehim, J. W. Keister, J. E. Rowe and T. E. Madey, *Prog. Surf. Sci.*, 1998, **59**, 117–134.
102 J. J. Kolodziej, T. E. Madey, J. W. Keister and J. E. Rowe, *Phys. Rev. B: Condens. Matter Mater. Phys.*, 2000, **62**, 5150–5162.
103 H.-S. Tao, J. E. Rowe and T. E. Madey, *Surf. Sci.*, 1998, **407**, L640–L646.
104 K. Pelhos, J. B. Hannon, G. L. Kellogg and T. E. Madey, *Surf. Sci.*, 1999, **432**, 115–124.
105 C.-H. Nien and T. E. Madey, *Surf. Sci.*, 1997, **380**, L527–L532.
106 C.-Z. Dong, L. Zhang, U. Diebold and T. E. Madey, *Surf. Sci.*, 1995, **322**, 221–229.
107 W. Chen and T. E. Madey, unpublished work.
108 W. Chen, P. Kaghazchi, T. Jacob and T. E. Madey, unpublished work.
109 E. D. Williams and N. C. Bartelt, *Science*, 1991, **251**, 393–400.
110 Z. Gai, R. G. Zhao, W. Li, Y. Fujikawa, T. Sakurai and W. S. Yang, *Phys. Rev. B: Condens. Matter Mater. Phys.*, 2001, **64**, 125201.
111 Z. Gai, W. S. Yang, R. G. Zhao and T. Sakurai, *Phys. Rev. B: Condens. Matter Mater. Phys.*, 1999, **59**, 15230–15239.
112 R. Plass, J. Feller and M. Gajdardziska-Josifovska, *Surf. Sci.*, 1998, **414**, 26–37.
113 M. Gajdardziska-Josifovska, R. Plass, M. A. Schofield, D. R. Giese and R. Sharma, *J. Electron Microsc.*, 2002, **51**, S13–S25.
114 U. Diebold, *Surf. Sci. Rep.*, 2003, **48**, 53–229.
115 A. C. Papageorgiou, C. L. Pang, Q. Chen and G. Thornton, *ACS Nano*, 2007, **1**, 409–414.
116 M. Reyhan, H. Wang and T. E. Madey, *Catal. Lett.*, in press.
117 K. Ohmori, Y. L. Foo, S. Hong, J. G. Wen, J. E. Greene and I. Petrov, *Nano Lett.*, 2005, **5**, 369–372.
118 J. R. Heffelfinger, M. W. Bench and C. B. Carter, *Surf. Sci.*, 1995, **343**, L1161–L1166.
119 R. Gabai, A. Ismach and E. Joselevich, *Adv. Mater.*, 2007, **19**, 1325–1330.
120 K.-B. Lee, E.-Y. Kim, C. A. Mirkin and S. M. Wolinsky, *Nano Lett.*, 2004, **4**, 1869–1872.
121 S. Benedetti, P. Torelli, P. Luches, E. Gualtieri, A. Rotaa and S. Valeri, *Surf. Sci.*, 2007, **601**, 2636–2640.
122 I. Ermanoski, PhD thesis, Rutgers University, 2005.